Yamazaki, Y., Stolle, C., Matzka, J., Siddiqui, T., Lühr, H., Alken, P. (2017): Longitudinal Variation of the Lunar Tide in the Equatorial Electrojet. - *Journal of Geophysical Research*, *122*, 12, pp. 12,445—12,463.

DOI: http://doi.org/10.1002/2017JA024601

AGU PUBLICATIONS

JGR

Journal of Geophysical Research: Space Physics

RESEARCH ARTICLE

10.1002/2017JA024601

Longitudinal Variation of the Lunar Tide in the Equatorial Electrojet

Yosuke Yamazaki[1], Claudia Stolle[1,2], Jürgen Matzka[1], Tarique A. Siddiqui[1,2,3], Hermann Lühr[1], and Patrick Alken[4,5]

[1]GFZ German Research Centre for Geosciences, Potsdam, Germany, [2]Institute of Earth and Environmental Science, University of Potsdam, Potsdam, Germany, [3]Now at High Altitude Observatory, National Center for Atmospheric Research, Boulder, CO, USA, [4]Cooperative Institute for Research in Environmental Sciences, University of Colorado Boulder, Boulder, CO, USA, [5]National Centers for Environmental Information, NOAA, Boulder, CO, USA

Key Points:
- Complete seasonal-longitudinal climatology is presented for the semidiurnal lunar tidal variation of the equatorial electrojet
- Significant longitudinal variation is found in the amplitude, while the variation in the phase is small
- Longitudinal variability can be partly explained by the effect of the inhomogeneous geomagnetic field

Correspondence to:
Y. Yamazaki,
yamazaki@gfz-potsdam.de

Citation:
Yamazaki, Y., Stolle, C., Matzka, J., Siddiqui, T. A., Lühr, H., & Alken, P. (2017). Longitudinal variation of the lunar tide in the equatorial electrojet. *Journal of Geophysical Research: Space Physics*, *122*, 12,445–12,463. https://doi.org/10.1002/2017JA024601

Received 17 JUL 2017
Accepted 4 NOV 2017
Accepted article online 10 NOV 2017
Published online 11 DEC 2017

Abstract The atmospheric lunar tide is one known source of ionospheric variability. The subject received renewed attention as recent studies found a link between stratospheric sudden warmings and amplified lunar tidal perturbations in the equatorial ionosphere. There is increasing evidence from ground observations that the lunar tidal influence on the ionosphere depends on longitude. We use magnetic field measurements from the CHAMP satellite during July 2000 to September 2010 and from the two Swarm satellites during November 2013 to February 2017 to determine, for the first time, the complete seasonal-longitudinal climatology of the semidiurnal lunar tidal variation in the equatorial electrojet intensity. Significant longitudinal variability is found in the amplitude of the lunar tidal variation, while the longitudinal variability in the phase is small. The amplitude peaks in the Peruvian sector (~285°E) during the Northern Hemisphere winter and equinoxes, and in the Brazilian sector (~325°E) during the Northern Hemisphere summer. There are also local amplitude maxima at ~55°E and ~120°E. The longitudinal variation is partly due to the modulation of ionospheric conductivities by the inhomogeneous geomagnetic field. Another possible cause of the longitudinal variability is neutral wind forcing by nonmigrating lunar tides. A tidal spectrum analysis of the semidiurnal lunar tidal variation in the equatorial electrojet reveals the dominance of the westward propagating mode with zonal wave number 2 (SW2), with secondary contributions by westward propagating modes with zonal wave numbers 3 (SW3) and 4 (SW4). Eastward propagating waves are largely absent from the tidal spectrum. Further study will be required for the relative importance of ionospheric conductivities and nonmigrating lunar tides.

1. Introduction

The atmospheric lunar tide is a global-scale oscillation of the Earth's atmosphere caused by the gravitational force of the Moon (Lindzen & Chapman, 1969). The dominant component of the lunar tide has a period of 12.421 h and is referred to as the semidiurnal lunar tide or M_2 tide. The M_2 tide is mostly generated near Earth's surface, and it propagates to higher altitude. Like other waves in the Earth's atmosphere (e.g., Yiğit & Medvedev, 2015), the amplitude of the lunar tidal wave increases with height, as the background atmospheric density exponentially decreases. The M_2 tidal amplitude peaks around 110 km altitudes, above which the wave is damped due to molecular dissipation. Ground-based radar observations have revealed that the M_2 tide in wind has an amplitude of several meters per second in the altitude range 80–110 km (Niu et al., 2005, 2007; Paulino et al., 2012, 2015; Sandford et al., 2006; Sathishkumar et al., 2017; Stening & Jacobi, 2001; Stening, Schlapp, et al., 1997; Stening & Vincent, 1989; Stening et al., 1987, 1990, 1994, 2003; Tsuda at al., 1981). More recent studies examined the global climatology of the M_2 tide in the upper atmosphere using satellite measurements (Forbes et al., 2013; Lieberman et al., 2015; Paulino et al., 2013; Zhang & Forbes, 2013).

The M_2 tide has also been numerically studied (Aso et al., 1981; Forbes, 1982a; Lindzen & Hong, 1974; Pedatella, Liu, Richmond, 2012; Stening, Forbes, et al., 1997; Stening et al., 1999; Vial & Forbes, 1994). Since the source gravitational field is well known, the lunar tidal forcing can be accurately prescribed in atmospheric models. Models' ability to predict the lunar tide depends on the accuracy of the background atmosphere used in the models, because the upward propagation of the lunar tide is largely controlled by the zonal mean

wind and temperature profiles. For this reason, lunar tidal observations are useful for assessing and improving atmospheric models.

The wind field in the ionospheric *E* region, or dynamo region (approximately 90–150 km), plays a crucial role in the ionospheric electrodynamics during daytime. At dynamo region heights, the ion-neutral collision frequency is comparable to or larger than the gyrofrequency of ions, while the electron-neutral collision frequency is much lower than the gyrofrequency of electrons. Accordingly, the motion of ions is dominated by the horizontal neutral wind while electrons are frozen to geomagnetic field lines. Different motions between ions and electrons give rise to electric currents, which result in a buildup of polarization charges and associated electric fields. The mechanism is referred to as the ionosphere wind dynamo (Richmond, 1979, 1989). The polarization electric fields generated in the *E* region are transmitted to the equatorial *F* region (>150 km) along equipotential magnetic field lines. These electric fields are usually eastward during daytime, and thus, at the magnetic equator where the geomagnetic field is horizontal, plasmas are transported vertically upward by the $\mathbf{E} \times \mathbf{B}$ drift (Alken, Chulliat, et al., 2013; Fejer et al., 1979, 2008). The lifted plasmas eventually diffuse downward and poleward along the geomagnetic field lines and produce the so-called equatorial anomaly crests at approximately $\pm 15^\circ$ from the magnetic equator (Hanson & Moffett, 1966; Moffett & Hanson, 1965). A number of observational studies have demonstrated the influence of the *E* region dynamo on the *F* region plasma distribution (Balan & Iyer, 1983; Dunford, 1967; Rastogi & Klobuchar, 1990; Rush & Richmond, 1973; Stolle et al., 2008). The dynamo process in the daytime *E* region is therefore important for understanding the behavior of the day-to-day weather of the whole ionosphere (Stening, 2003).

Under steady state conditions, the dynamo current **J** relates to the ionospheric conductivity tensor $\hat{\sigma}$, electric field **E**, neutral wind **U**, and background geomagnetic field **B** as follows (Richmond, 1995):

$$\mathbf{J} = \hat{\sigma} \cdot (\mathbf{E} + \mathbf{U} \times \mathbf{U}) . \tag{1}$$

The ionospheric conductivity varies with the plasma density, which causes a solar cycle variation in the current (Takeda, 1999, 2013; Takeda et al., 2003). The ionospheric conductivity also tends to vary inversely with the magnitude of the background geomagnetic field. Numerical studies have shown that an increase in the magnitude of the background geomagnetic field leads to a reduction of the current, as the decrease in the conductivity is more significant than the increase in the electromotive force $\mathbf{U} \times \mathbf{B}$ (Cnossen et al., 2012; Takeda, 1996). *E* region currents essentially vanish during nighttime because of the small ionospheric conductivity.

The neutral wind in the dynamo region is usually dominated by atmospheric solar tides (Forbes et al., 2008; Oberheide et al., 2011), which are thermally excited by solar heating. Model calculations have shown that the solar tides are primarily responsible for the formation of the global-scale ionospheric current system, commonly known as solar quiet (S_q) current system (Forbes & Lindzen, 1976; Matsushita, 1969; Miyahara & Ooishi, 1997; Richmond et al., 1976; Stening, 1969; Takeda & Maeda, 1980, 1981, Tarpley, 1970a). The solar tides at dynamo region heights are a superposition of the waves that are locally generated in the thermosphere and those that propagate into the dynamo region from the lower atmosphere (Forbes, 1982b; Hagan et al., 2001). The tides from the lower atmosphere accounts for up to 50% of the ionospheric wind dynamo currents (Richmond & Roble, 1987; Yamazaki, Richmond, Maute, Wu, et al., 2014).

The zonal current density is strongly enhanced near the magnetic equator (say, within $\pm 3^\circ$ magnetic latitudes), where the effective zonal conductivity is locally elevated owing to the so-called Cowling effect (Baker & Martyn, 1953; Hirono, 1950). The enhanced eastward current flow along the magnetic equator is commonly known as the equatorial electrojet. Spatial and temporal characteristics of the S_q current system and equatorial electrojet have been extensively studied on the basis of magnetometer data analysis as well as numerical models (see a review by Yamazaki & Maute, 2017).

The M_2 tide modulates the S_q current system and equatorial electrojet by driving an additional ionospheric current system, known as the lunar (*L*) current system (Çelik, 2014; Malin, 1973; Matsushita & Xu, 1984). Numerical calculations verified that the *L* current system can result from the dynamo action by lunar tidal winds (Maeda & Fujiwara, 1967; Tarpley, 1970b). The total current intensity of *L* is usually about one tenth of the total S_q current intensity (Yamazaki et al., 2011), but the relative contribution of *L* may vary significantly from day to day. The magnetic effect of the M_2 tide is most evident near the magnetic equator, where horizontal magnetic perturbations are enhanced due to the equatorial electrojet (Bartels & Johnston, 1940; Onwumechilli & Alexander, 1959; Raja Rao & Sivaraman, 1958). The mechanism by which neutral winds affect

the equatorial electrojet has been discussed in various articles (e.g., Hysell et al., 2002; Richmond, 1973; Stening, 1995; Yamazaki, Richmond, Maute, Liu, et al., 2014). The modulation of the *E* region dynamo due to the M_2 tide also causes similar tidal oscillations in the equatorial vertical $\mathbf{E} \times \mathbf{B}$ plasma drift velocities (Fejer & Tracy, 2013; Stening & Fejer, 2001; Tarpley & Balsley, 1972) and in the *F* region plasma densities near the equatorial anomaly crests (Bhuyan & Tyagi, 1986; Matsushita, 1967; Rastogi et al., 1985; Paulino et al., 2017; Pedatella, 2014; Pedatella & Forbes, 2010). Eccles et al. (2011) were able to reproduce the day-to-day variability observed simultaneously in the equatorial electrojet and *F* region plasma density by including the semidiurnal lunar tide in an ionospheric wind dynamo model.

It has been suggested in recent studies that the lunar tide plays a significant role in producing large perturbations in the equatorial ionosphere during stratospheric sudden warming events. A stratospheric sudden warming event is a large-scale meteorological disturbance in the middle atmosphere, which usually takes place in the arctic region during the winter (Andrews et al., 1987; Labitzke & van Loon, 1999). The lunar tidal variation in the equatorial electrojet has been observed to amplify during stratospheric sudden warming events (Fejer et al., 2010; Park et al., 2012; Siddiqui, Lühr, et al., 2015; Siddiqui, Stolle, et al., 2015; Yamazaki, 2013; Yamazaki, Richmond, et al., 2012; Yamazaki, Yumoto, et al., 2012). Numerical studies (Forbes & Zhang, 2012; Stening, Forbes, et al., 1997) clarified the sensitivity of the M_2 tide to the zonal mean background atmosphere during stratospheric sudden warmings. They have shown that stratospheric sudden warming events produce favorable conditions for the vertical propagation of the M_2 tide from the lower atmosphere to the upper atmosphere, which results in an amplification of the M_2 tide in the lower thermosphere. Simulations based on coupled thermosphere-ionosphere models have demonstrated that the enhanced M_2 tide during stratospheric sudden warming events can produce large perturbations in the equatorial electric field (Maute et al., 2016; Pedatella & Liu, 2013; Pedatella, Liu, Richmond, et al., 2012; Pedatella et al., 2012, 2014).

Recently, Siddiqui et al. (2017) reported that the amplitude of the lunar tidal variation in the equatorial electrojet intensity is greater in the Peruvian sector than in the Indian sector during the major stratospheric sudden warming events of 2006 and 2009. They also found a similar longitudinal dependence in the lunar tidal amplitude during the winter of 2007 when there was no stratospheric sudden warming event. The longitudinally inhomogeneous lunar tidal effect in the equatorial electrojet has also been reported by Rastogi and Trivedi (1970) and Gupta (1973), and more recently by Stening (2011) and Yizengaw and Carter (2017). Rastogi and Trivedi (1970) and Stening (2011) showed that the longitudinal variability could be seasonally dependent. Despite increasing evidence of the longitudinal variability, its zonal structure and seasonal characteristics are largely unknown due to limited spatial and temporal coverage of ground measurements used in the previous studies. The present study, on the basis of global satellite measurements, aims to determine the complete seasonal-longitudinal climatology of the lunar tide in the equatorial electrojet.

Lühr et al. (2012) examined the dependence of the equatorial electrojet intensity on the lunar phase using decade-long magnetometer data from the CHAMP satellite. Although they addressed the influence of solar cycle and season on the lunar tidal variation of the equatorial electrojet, the longitudinal variability was not examined in detail. The present study is to improve our understanding of the lunar tidal variation in the equatorial electrojet by fully addressing its dependence on longitude. To this end, we will explore an extended data set that combines 10 years of CHAMP measurements with more recent measurements from two Swarm satellites over a 3 year period.

Alken and Maus (2007) presented empirical models of the equatorial electrojet intensity, EEJM. Version 1.0 of the EEJM includes the dependence on solar activity, season, local time, and longitude. Later, version 2.0 was released (Alken, 2009), which incorporates the dependence on lunar time as well. For each version of the EEJM, there are three independent models based on three different satellite measurements from CHAMP, Ørsted, and SAC-C. We call them EEJM (CHAMP), EEJM (Ørsted), and EEJM (SAC-C), respectively. Although the lunar time parameterization used in version 2.0 allows the models to reproduce the semidiurnal lunar variation, its seasonal-longitudinal climatology has not been studied in detail. We will make comparisons between the results of our data analysis and model predictions by version 2.0 of the EEJM (CHAMP) and EEJM (Ørsted). The SAC-C model will not be used in this study, because it does not include the dependence on local time owing to the Sun-synchronous orbit of the satellite.

The longitudinal variation of the mean equatorial electrojet intensity is well known. Early studies based on ground measurements suggested that the longitudinal variation of the equatorial electrojet is dominated by the conductivity effect, so that the intensity varies inversely with the strength of the background geomagnetic

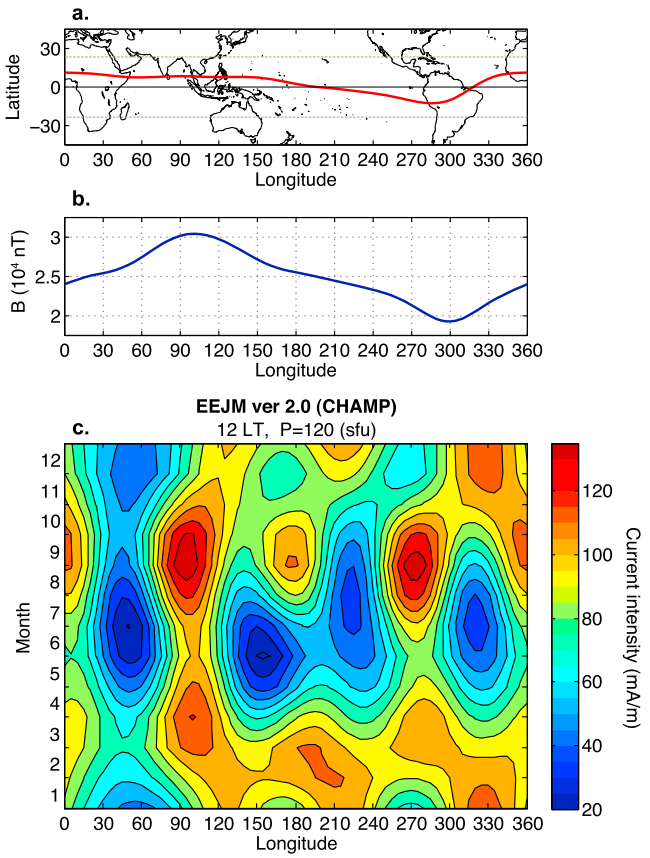

Figure 1. Longitudinal variations in (a) the location of the magnetic equator and (b) the background geomagnetic field strength at the magnetic equator. (c) Seasonal and longitudinal dependence of the noontime equatorial electrojet intensity, derived from version 2.0 of the EEJM (CHAMP) for $P = 120$ sfu for the mean lunation.

field (Doumouya et al., 2003; Rastogi, 1962). Later studies involving satellite measurements established a more comprehensive longitudinal structure of the equatorial electrojet (Alken & Maus, 2007; England et al., 2006; Le Mouël et al., 2006; Lühr & Manoj, 2013; Lühr et al., 2004). Figure 1c reveals the seasonal-longitudinal climatology of the noontime equatorial electrojet intensity derived from version 2.0 of the EEJM (CHAMP). The model calculations were made for the mean lunation for a moderate solar activity condition with the solar activity index P (Richards et al., 1994) being 120 solar flux unit (sfu = 10^{-22} W m^{-2} Hz^{-1}). The P index was derived from the observed solar radio noise flux at a wavelength of 10.7 cm (the so-called $F_{10.7}$) (Tapping, 2013). It is immediately obvious that the background geomagnetic field strength, shown in Figure 1b, cannot fully explain the longitudinal variation of the mean equatorial electrojet intensity. For instance, the strength of the background geomagnetic field over the magnetic equator peaks around 100°E, which is expected to result in a weak equatorial electrojet due to the inverse relationship between the field strength and ionospheric conductivities. However, the equatorial electrojet in this longitude sector is rather strong throughout the year. It is now widely accepted that the longitudinal variation of the mean equatorial electrojet intensity is primarily due to longitudinally inhomogeneous solar tidal forcing (England et al., 2006; Fang et al., 2009; Jin et al., 2008; Lühr et al., 2008; Pedatella, Hagan, et al., 2012; Lühr & Manoj, 2013). Nonmigrating (i.e., not Sun-synchronous) tides are responsible for the forcing that varies with longitude.

Most previous studies on the atmospheric lunar tide focused on the migrating (i.e., Moon-synchronous) component (Forbes et al., 2013; Lieberman et al., 2015; Zhang & Forbes, 2013). An exception is the work by Paulino et al. (2013), which took into account possible contributions by nonmigrating (i.e., not Moon-synchronous) tides. They performed a spectrum analysis of the M_2 tide in the temperature data taken from the Sounding of the Atmosphere using Broadband Emission Radiometry (SABER) instrument on board the Thermosphere Ionosphere Mesosphere Energetics Dynamics (TIMED) satellite. The zonal wave number spectrum they obtained from the composite data (2002–2012) during December at 108 km indicated the dominance of the migrating component, which is the westward propagating mode with zonal wave number 2 (SW2). The results by Paulino et al. (2013) also revealed the existence of nonmigrating components; specifically, eastward propagating modes with zonal wave numbers 1 (SE1) and 2 (SE2), and westward propagating modes with zonal wave numbers 5 (SW5) and 6 (SW6). These nonmigrating tides can cause longitudinal variability of the semidiurnal lunar variation in the equatorial electrojet. We will address this possibility by applying the same tidal spectrum analysis to the lunar tidal variation of the equatorial electrojet.

2. Data, Model, and Method of Analysis

2.1. CHAMP

The German satellite CHAMP was launched in the year 2000 into a near-polar orbit with an initial altitude of ~450 km (Reigber et al., 2002). CHAMP provided high-precision magnetic field measurements over a 10 year period until the reentry in 2010. The CHAMP magnetometer data have been used for studying various aspects of low- and middle-latitude ionospheric currents (e.g., Alken et al., 2011; Lühr & Maus, 2006; Maus & Lühr, 2006; Manoj et al., 2006; Park et al., 2011; Pedatella et al., 2011).

The satellite completes an orbit every ~92 min. The orbital plane slowly processes through local time at the rate of ~5.44 min/d. It takes 131 days to sample all local times between 0600 and 1800 LT. The equatorial electrojet intensity was derived for each equatorial crossing basically following the technique detailed in Lühr et al. (2004). The technique has been revised, following Alken, Maus, et al. (2013), by taking into account the realistic geometry of the magnetic equator, along which the equatorial electrojet is assumed to flow. The data were used for the entire duration of the satellite operation, from July 2000 to September 2010.

2.2. Swarm

European Space Agency (ESA)'s satellite constellation Swarm consists of three satellites, namely, Swarm A, Swarm B, and Swarm C (Friis-Christensen et al., 2006, 2008). It was launched into a near polar orbit in November 2013. Each satellite carries a magnetometer. The accuracy of the Swarm magnetometers is comparable with that of the CHAMP magnetometer. The Swarm magnetometer data have been used to study low- and middle-latitude ionospheric currents (Alken, 2016; Alken et al., 2015; Chulliat et al., 2016; Lühr et al., 2015).

The Swarm A and Swarm C satellites fly side by side at an altitude of ~460 km with inclinations of 87.4°, while the Swarm B satellite flies at a higher altitude of ~530 km with an inclination of 88°. The equatorial electrojet intensity was calculated using the technique detailed in Alken, Maus, et al. (2013). We used the data from Swarm A and Swarm B observed during the period from November 2013 to February 2017.

2.3. Retrieval of Lunar Tidal Variation

The procedure of determining the lunar tidal variation in the equatorial electrojet intensity consists of the following steps. First, we excluded the data corresponding to the periods of relatively high geomagnetic activity ($K_p > 3^+$). Our test revealed that the results presented in this paper are not particularly sensitive to the choice of this K_p criteria. Second, we evaluated the mean equatorial electrojet intensity using version 1.0 of the EEJM (CHAMP) and subtracted it from the corresponding data. The EEJM considers the (solar) local time dependence of the equatorial electrojet, and hence solar tidal influences are essentially removed from the data. Besides, remaining solar tidal signatures will largely cancel out at a later stage when the residual data (i.e., data minus model) are sorted according to the lunar time. Since version 1.0 of the EEJM does not include the lunar dependence, the effect of the lunar tide may be found in the residuals.

Next, the residuals were divided into subgroups based on solar activity, season, solar time, and longitude. Several different ways of data binning were used to illustrate different features of the lunar tidal variation. Details of our binning procedure will be explained later. Finally, the amplitude A and phase ϕ of the semidiurnal lunar tidal component were determined using a Fourier technique. We defined the phase to be the lunar time when the semidiurnal tidal variation peaks within ±6 h lunar time. 1 σ errors were evaluated for A and ϕ using the bootstrap method (Efron, 1981).

3. Results and Discussion

3.1. Longitudinally Independent Component

We first examine the longitudinally independent component of the lunar tidal variation. The analysis was performed separately for each bihourly solar time bin. The seasonal dependence was taken into account by binning the residuals into three seasonal bins: J months (May–August), E months (March, April, September, October), and D months (November–February). The residual data were further divided for higher ($P \geq 100$ sfu) and lower ($P < 100$ sfu) solar activity conditions. The residual data in each group were separated into 12 one hour lunar time bins. At each lunar time, the mean value was calculated with equal weighting for different longitudes. Finally, least squares sinusoidal fits were performed to extract the semidiurnal lunar tidal signal.

Figure 2 gives examples of the semidiurnal lunar variation determined by the method detailed above. The results are presented for noontime (between 1100 and 1300 solar time) under different seasonal and solar activity conditions. The dot data points in each panel are the mean values at each hourly lunar time bin, and the vertical bars represent 1 standard deviation of the corresponding data sample on either side of the mean values (not standard error of the mean). The large error bars are due to short-term (i.e., hour-to-hour and day-to-day) variability of the equatorial electrojet, which can result from highly variable wave forcing from the lower and middle atmosphere (Kawano-Sasaki & Miyahara, 2008; Yamazaki, Richmond, Maute, Liu, et al., 2014). The short-term variability of the equatorial electrojet is not considered in the EEJM and thus remains in the residual data. The line curve in each panel shows the least squares sinusoidal fit to the 12 mean values, which represents the semidiurnal lunar variation. The amplitude A and phase ϕ of the semidiurnal lunar variation can be found in each panel along with the corresponding 1 σ errors (σ_A and σ_ϕ, respectively). Moreover, the correlation coefficient R, evaluated for fitting, is indicated in each panel.

The results in Figure 2 reveal a strong dependence of the lunar tidal amplitude on season. In both higher and lower solar activity cases, the amplitude during the D months is approximately twice as large as that during the J months. The strong lunar tidal effect during the Northern Hemisphere winter has been known for many years (e.g., Bartels & Johnston, 1940). It may also be noted that the amplitude is greater in the higher solar activity case than in the lower solar activity case at the same season. The solar activity dependence

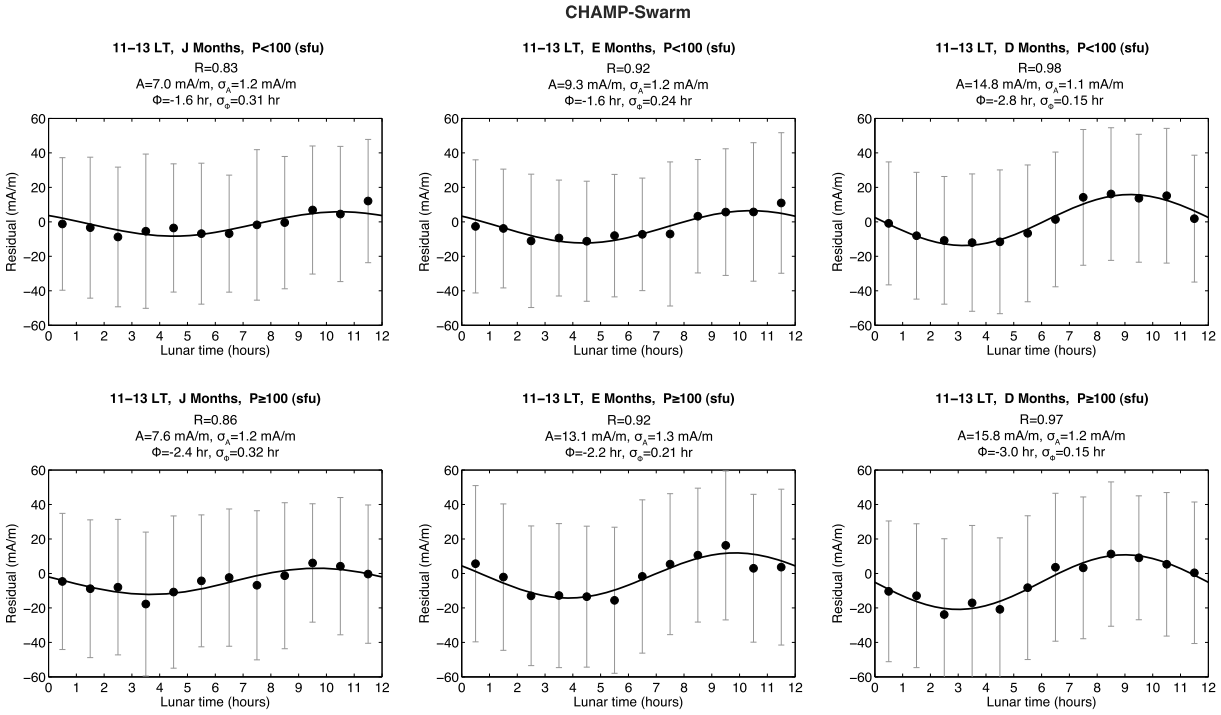

Figure 2. Examples of least squares fits of the semidiurnal curve to the hourly mean values of the residual equatorial electrojet intensities. The results are presented here for the solar local times between 1100 and 1300. Shown are the (top row) lower ($P < 100$ sfu) and (bottom row) higher ($P \geq 100$ sfu) solar activity cases. Also shown are the (left column) J months, (middle column) E months, and (right column) D months. The data points in each panel are the mean values within each lunar hourly bin, and vertical bars are the standard deviations of the data on each side of the mean.

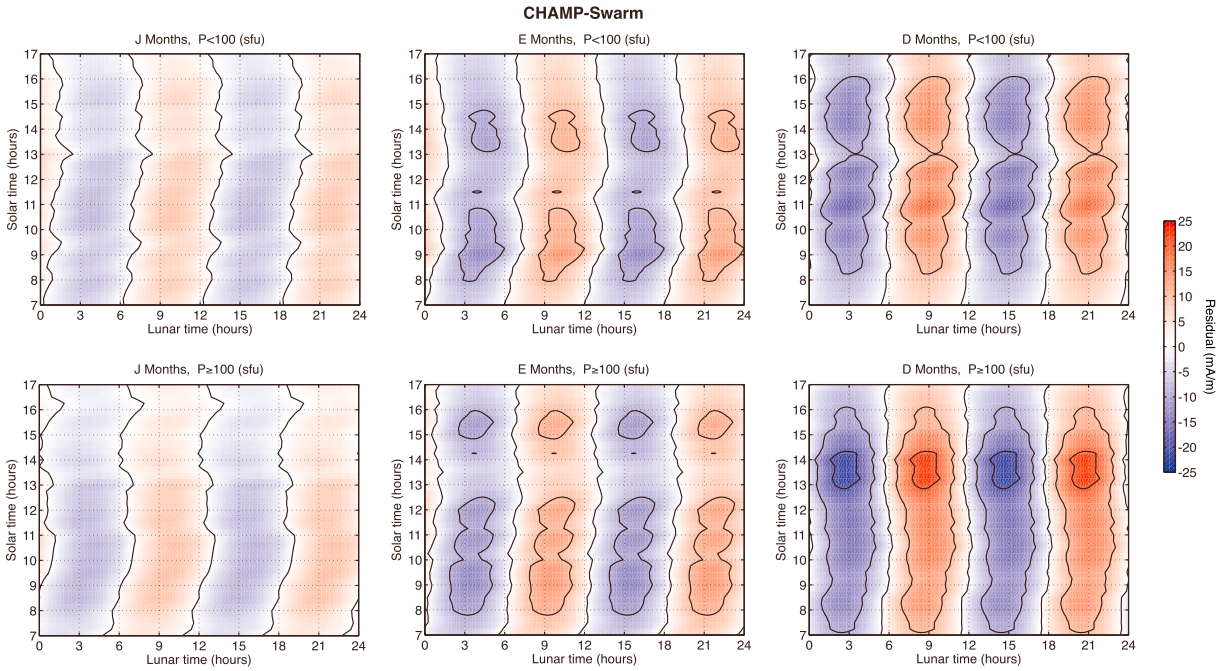

Figure 3. Lunar semidiurnal variations in the equatorial electrojet intensity as a function of solar time and lunar time. Shown are the (top row) lower ($P < 100$ sfu) and (bottom row) higher ($P \geq 100$ sfu) solar activity cases. Also shown are the (left column) J months, (middle column) E months, and (right column) D months.

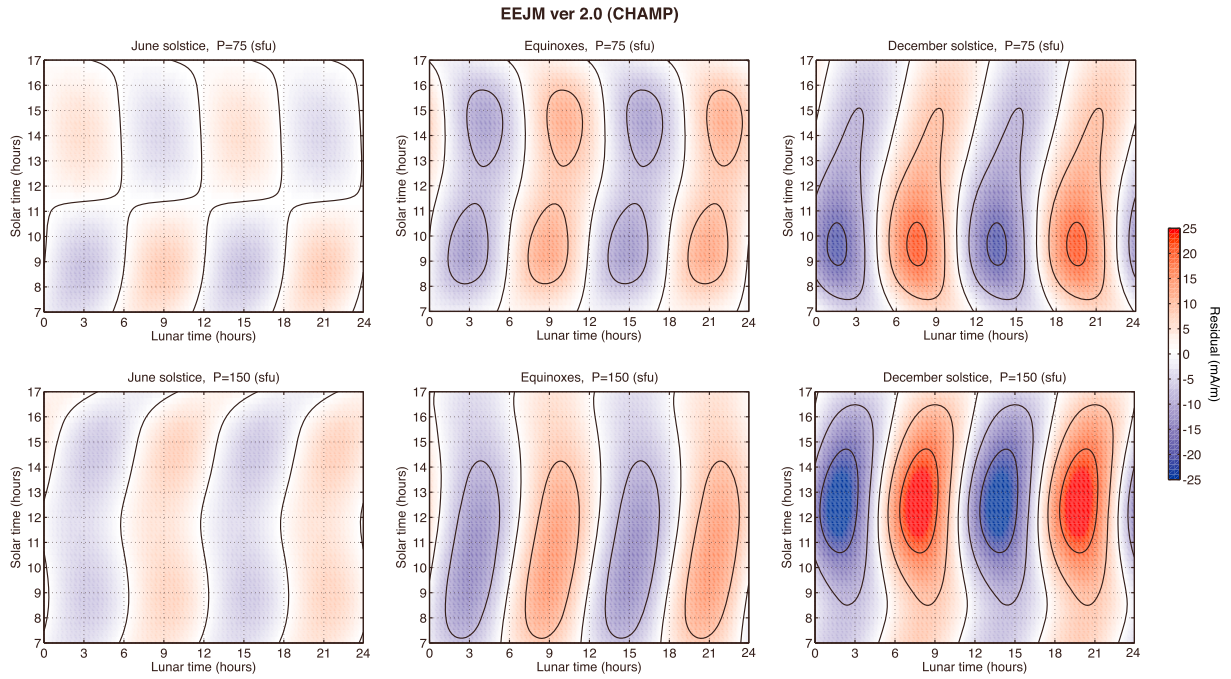

Figure 4. Similar to Figure 3, but the results are derived from version 2.0 of the EEJM (CHAMP) for (top row) $P = 75$ sfu and (bottom row) $P = 150$ sfu, and for the (left) June solstice, (middle) equinoxes, and (right) December solstice.

can be attributed to the effect of enhanced ionospheric conductivity during solar maximum periods. Lühr et al. (2012) showed that the sensitivity of the lunar tidal amplitude to solar activity is similar to that of the mean equatorial electrojet intensity, so that the ratio of the lunar tidal amplitude to the mean equatorial electrojet intensity tends to be the same in different solar activity conditions.

Figure 3 presents the semidiurnal lunar variation as a function of solar time for different seasonal and solar activity conditions. It can be seen in each case that the phase of the lunar tidal variation is largely the same at different solar times. It can also be noted that there is a shift in the phase of the semidiurnal lunar variation to earlier lunar time by 1 h or so during the D months. Matsushita and Xu (1984) found a similar phase shift in the *L* current system at middle and low latitudes. Thus, the seasonal phase shift is likely due to changes in the global lunar tidal wind system.

Figures 4 and 5 are similar to Figure 3 but show the results derived from version 2.0 of the EEJM (CHAMP) and EEJM (Ørsted), respectively. The results are longitudinally averaged and shown for the June solstice (day of year DoY = 172) and the December solstice (DoY = 355), as well as for the equinoxes, which is the average of the results for the March equinox (DoY = 80) and September equinox (DoY = 264). The results are also presented separately for the solar activity index $P = 75$ sfu and $P = 150$ sfu, which correspond approximately to the average values of the *P* index for the higher ($P \geq 100$ sfu) and lower ($P < 100$ sfu) solar activity cases considered in Figures 2 and 3. Comparisons with the CHAMP-Swarm results in Figure 3 reveal that both models reproduce the main features of the semidiurnal lunar variation. The lunar tidal amplitudes derived from the models are generally in good agreement with the observations. The models also reproduce the seasonal variation in the amplitude. That is, the amplitude is largest during the Northern Hemisphere winter and smallest during the Northern Hemisphere summer. Some differences exist between the data and model, especially in the phase of the semidiurnal lunar variation. In some cases, the phase of the semidiurnal lunar variation varies with solar time (e.g., the CHAMP model results in Figure 4 for the June solstice with $P = 75$ sfu). Such variations are not seen in Figure 2, and thus, they could be erroneous features in the model caused by insufficient data coverage.

3.2. Longitudinal Dependence

Next, we examine the longitudinal dependence of the semidiurnal lunar variation. The investigation requires longitudinal binning in addition to the data separation based on solar time, season, and solar activity. In order to have a sufficient volume of data in each longitudinal bin, solar time and solar activity binnings were

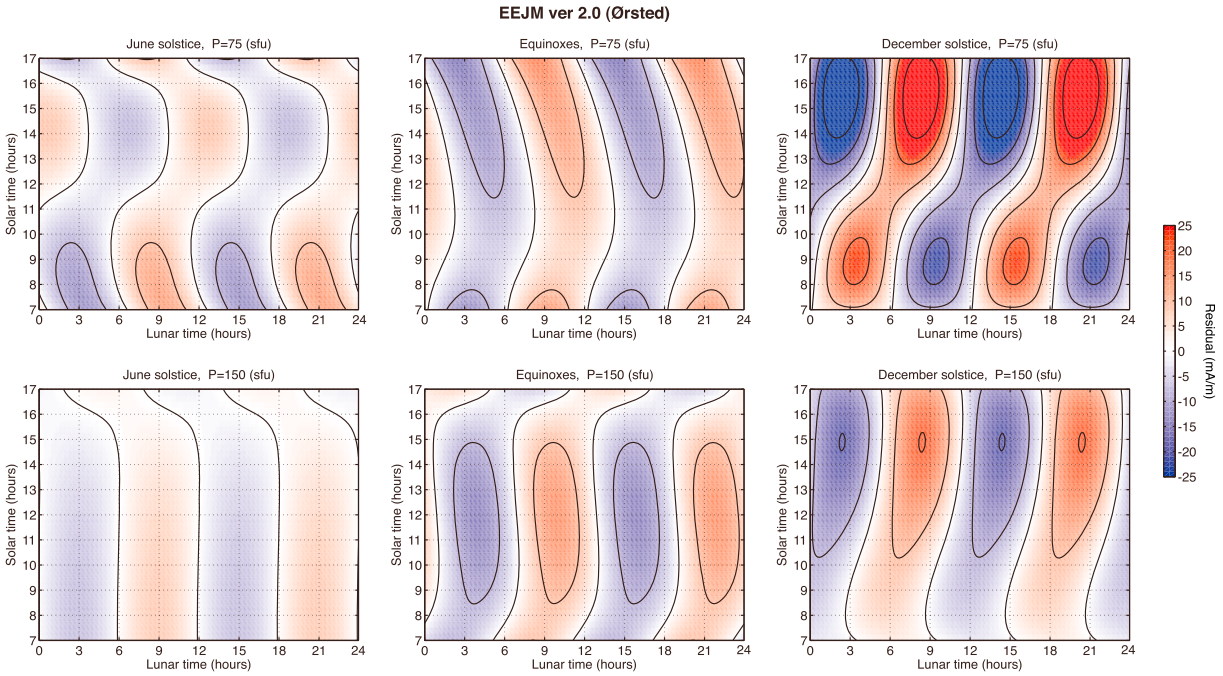

Figure 5. Similar to Figure 3, but the results are derived from version 2.0 of the EEJM (Ørsted) for (top row) $P = 75$ sfu and (bottom row) $P = 150$ sfu, and for the (left) June solstice, (middle) equinoxes, and (right) December solstice.

modified as described below. The analysis of the semidiurnal lunar variation was performed for the following four cases. In the first two cases, the residual data were separated into two groups based on solar time regardless of solar activity (i.e., the P index). That is, the "morning" case involves the data between 0800 and 1200 h solar time and the "afternoon" case includes the data between 1200 and 1600 h solar time. In the other two cases, the residual data were divided into two groups based on the solar activity index P for all solar times between 0800 and 1600. The "solar maximum" case involves the residual data for $P \geq 100$ sfu and the "solar minimum" case for $P < 100$ sfu. For each group of data, the longitudinal dependence was obtained by binning the residual data within $\pm 15°$ window and moving it forward in longitude by 5° at a time.

Examples of least squares fits to the residual data are depicted in Figure 6. Figure 6 (left column) is for the J months (May–August) for the solar minimum case. The to panel shows the results obtained for 230–260°E longitudes, while the bottom panel shows the results for 310–340°E longitudes. These longitude sectors correspond to where the amplitude of the semidiurnal lunar variation was found to be smallest and largest, respectively. The amplitude in the Brazilian region (310–340°E longitudes) is approximately 5 times as large as that in the central Pacific region (230–260°E longitudes). The amplitude difference is significant, while the difference in the phase is not significant when the 1 σ error is taken into account. Figure 6 (middle column) is for the E months (March, April, September, October) for the solar maximum case. The top panel is for the longitude sector where the amplitude is smallest, while the bottom panel is for where the amplitude is largest. Again, there is a significant difference in the amplitude between the two regions. Figure 6 (right column) is for the D months (November–February) for the morning case. The amplitude is largest in the Peruvian region (270–300°E longitudes) and smallest in the Central Pacific region (170–200°E longitudes).

Figure 7 shows the longitudinal variations in the amplitude and phase of the semidiurnal lunar variation. In each panel, different colored lines indicate the results obtained using different binning methods (i.e., morning, afternoon, solar maximum, and solar minimum). The black line represents the case that includes all solar times between 0800 and 1600 and all solar activity levels. It can be seen that significant longitudinal variability exists in the amplitude, while the variability in the phase is rather small (~1 h) compared to the full-scale range of ±6 h. Siddiqui et al. (2017), comparing the lunar tidal signal between the Peruvian and Indian sectors, also noted that the phases in the two regions were similar despite a significant difference in the amplitudes. It can also be seen in Figure 7 that for each season, the longitudinal variations of the lunar tidal amplitude derived

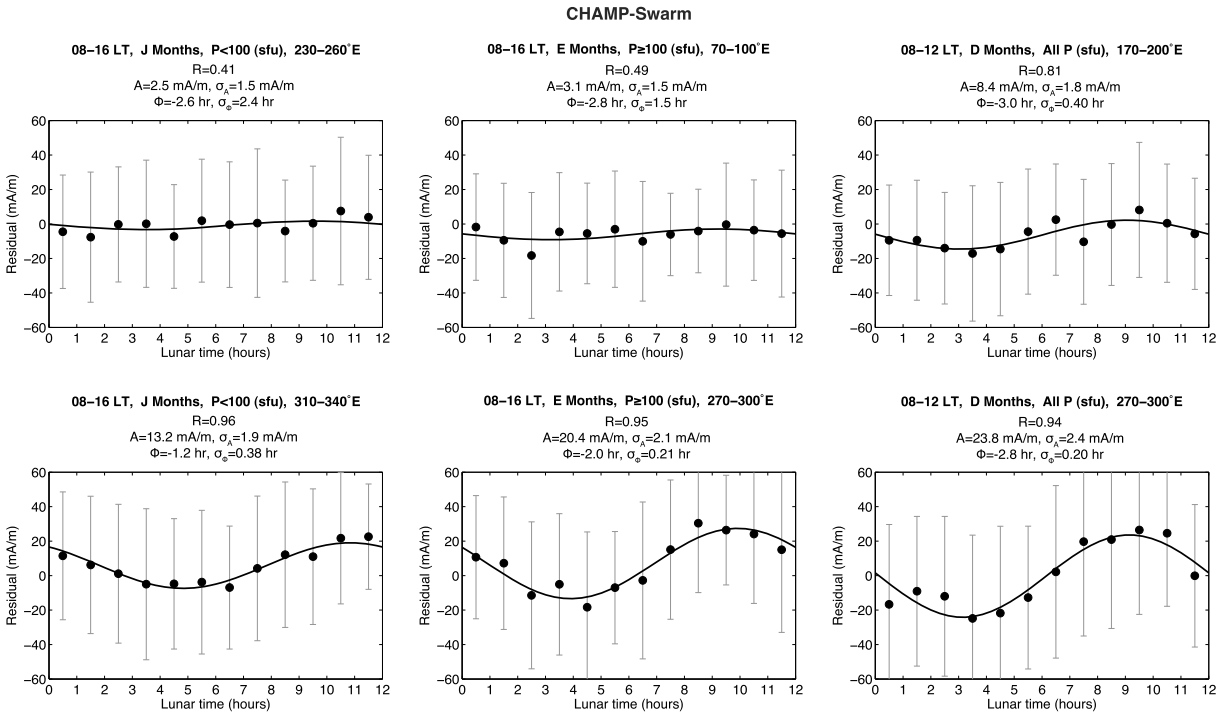

Figure 6. Similar to Figure 2 but for different binning cases. The panels are for the (left column) J months of the solar minimum case, (middle column) E months of the solar maximum case, and (right column) D months of the morning case. See text for binning details. The results are shown for the longitudes where the amplitude is (top row) smallest and (bottom row) largest.

with different binning methods are similar, indicating that the longitudinal pattern is essentially the same at different solar times and solar activity levels.

During the E months, the amplitude of the semidiurnal lunar variation is largest in the Peruvian region (270–300°E longitudes) and smallest in the Indian region (70–100°E longitudes) (Figures 6 and 7). The pattern

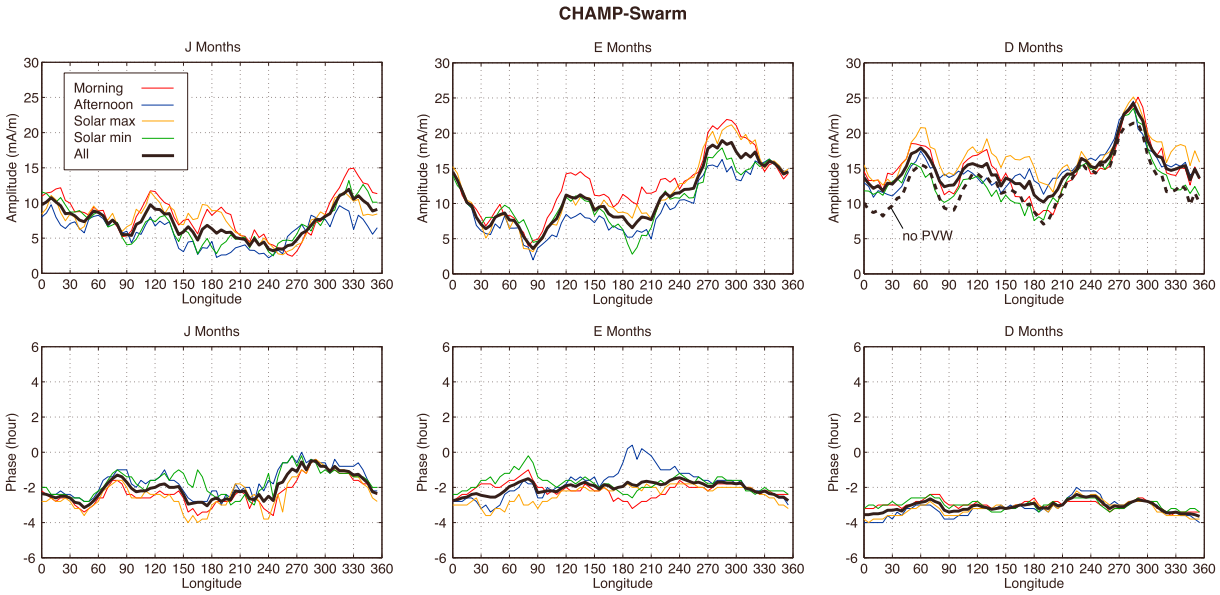

Figure 7. Longitudinal variations of the (top row) amplitude and (bottom row) phase of the semidiurnal lunar variation in the equatorial electrojet intensity for the (right column) J months, (middle column) E months, and (right column) D months. Different colored lines indicate the results obtained for different binning cases (i.e., morning, afternoon, solar maximum, and solar minimum). For the amplitude during the D months shown in Figure 7 (top right), the results are also indicated for the no-PVW case, which excludes the data during stratospheric sudden warming events. See text for binning details.

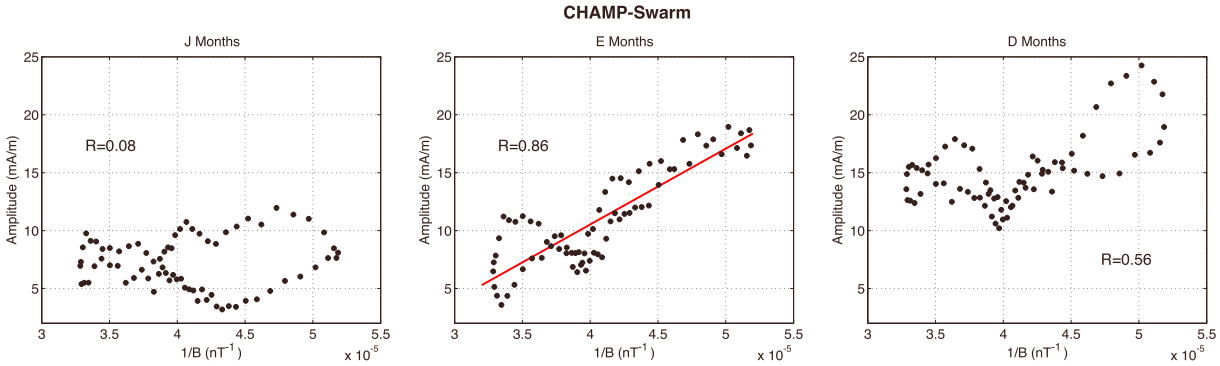

Figure 8. Scatterplots of the amplitude of the semidiurnal lunar variation and the reciprocal of the background geomagnetic field strength for the (left) J months, (middle) E months, and (right) D months.

is the opposite of the background geomagnetic field strength, which is largest in the Indian region and smallest in the Peruvian region (see Figure 1b). A possible explanation of this anticorrelation is the effect of the ionospheric conductivity that varies inversely with the strength of the background geomagnetic field. Scatter plots for the amplitude of the semidiurnal lunar variation and the reciprocal of the background geomagnetic field strength are shown in Figure 8. The high correlation ($R = 0.86$) during the E months suggests that the conductivity effect plays a role for the longitudinal variation of the lunar tidal amplitude during these months. The correlation is lower during the solstices, thus other mechanisms may also be involved. Strictly speaking, the equatorial electrojet intensity tends to scale with $|\mathbf{B}|^{-2/3}$, rather than $|\mathbf{B}|^{-1}$ (Cnossen, 2017; Glassmeier et al., 2004; Matzka et al., 2017). We noted that the use of $|\mathbf{B}|^{-2/3}$, instead of $|\mathbf{B}|^{-1}$, makes little difference in the correlation results.

Another possible cause of the longitudinal variation is the geometry of the magnetic equator. According to the angle between the geographic and magnetic equators (denoted here as θ_g), the way the neutral winds affect the equatorial electrojet can be different. Let u and v represent the zonal and meridional winds, respectively. The neutral wind component parallel to the equatorial electrojet is $u\cos\theta_g + v\sin\theta_g$ and the perpendicular component is $v\cos\theta_g - u\sin\theta_g$. Thus, even if u and v are independent of longitude, the effect of the neutral wind on the equatorial electrojet can vary with longitude because of θ_g. However, given the small longitudinal variation of θ_g (mostly within the range between −10°and 30°), this mechanism is unlikely to explain the longitudinal variation of the semidiurnal lunar tidal amplitude in the equatorial electrojet, which exceeds 100% at some longitudes.

Next, we examine the relationship between the longitudinal variations of the lunar tidal amplitude and the mean (background) equatorial electrojet intensity. The results are presented in Figure 9. Using version 2.0 of the EEJM (CHAMP), the mean equatorial electrojet intensity was derived as the average of the equatorial electrojet intensities calculated for different solar times (0800–1600) and different solar activity conditions ($P = 75$–150 sfu) for the mean lunation. No obvious correlation exists between the lunar tidal amplitude and the mean equatorial electrojet intensity, which indicates that different mechanisms dominate the longitudinal variability of the two parameters. As mentioned earlier, the longitudinal variation of the mean equatorial

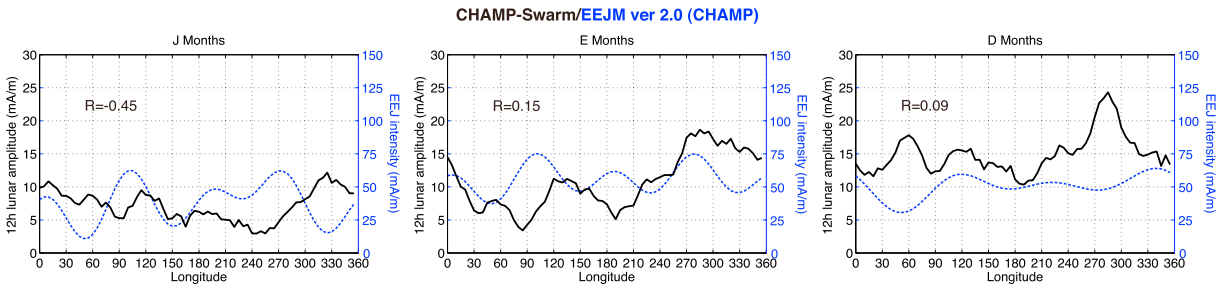

Figure 9. Longitudinal variations in (black) the amplitude of the semidiurnal lunar variation in the equatorial electrojet intensity and (blue) the mean equatorial electrojet intensity derived from version 2.0 of the EEJM (CHAMP) for the (left) J months, (middle) E months, and (right) D months. The lunar tidal amplitude and the mean equatorial electrojet intensity are given on the left and right side of the vertical axis in each panel, respectively.

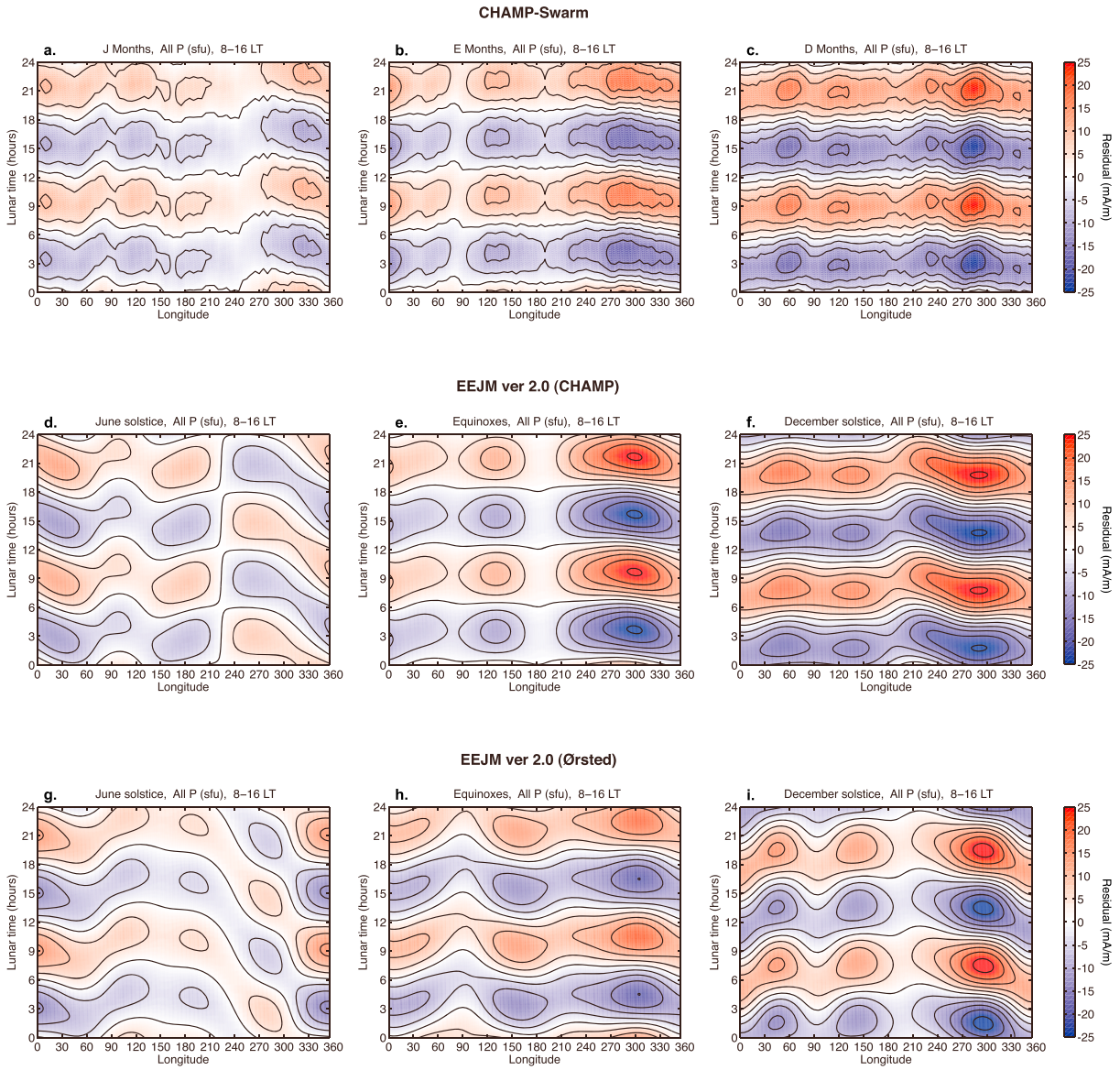

Figure 10. Lunar semidiurnal variations in the equatorial electrojet intensity as a function of lunar time and longitude for the (left column) J months, (middle column) E months, and (right column) D months. The results are obtained from the (a–c) CHAMP-Swarm data, (d–f) EEJM (CHAMP), and (g–i) EEJM (Ørsted).

electrojet intensity is mainly due to nonmigrating solar tides, which would have little effect on the semidiurnal lunar variation of the equatorial electrojet.

The lunar tidal amplitude is known to undergo a significant enhancement during stratospheric sudden warming events, which occur mostly during the D months. Therefore, it is possible that the longitudinal variation of the amplitude during the D months may be influenced by such extreme events. In order to address the possible effect of stratospheric sudden warming events, a separate analysis was performed for the D months using a data set that includes all solar times between 0800 and 1600 and all solar activity levels but excludes the periods of stratospheric sudden warming events. The identification of stratospheric sudden warming events was based on the concept of polar vortex weakening (PVW), proposed by Zhang and Forbes (2014). PVW is defined by a reduction of the zonal mean zonal wind at 70°N at 1 hPa (~48 km altitude) during the Northern Hemisphere winter, which is associated with dynamical changes in the middle atmosphere during arctic stratospheric sudden warming events. Studies have shown that there is a good correlation between PVW and semidiurnal lunar tidal activity in the lower thermosphere (Chau et al., 2015; Zhang & Forbes, 2014) as well as in the equatorial electrojet (Siddiqui, Stolle, et al., 2015) in terms of timing and intensity. The peak times

of PVW were tabulated by Yamazaki et al. (2015) for the years 1967–2013 based on the zonal mean zonal wind obtained from the ERA-40 (1966–1978) (Uppala et al., 2005) and ERA-Interim (1979–2014) (Dee et al., 2011). The same list was used in the present study, but it was extended to March 2017. The data were excluded for 30 days (i.e., one lunar cycle) starting from 5 days prior to the peak PVW. The dashed line in Figure 7 (top right) shows the longitudinal variation of the lunar tidal amplitude, derived from this data set ("no PVW"). As expected, the lunar tidal amplitude is smaller at all longitudes when the data during PVW (and hence stratospheric sudden warming events) are eliminated. Nonetheless, there is little difference in the longitudinal pattern between the results including and excluding PVW. Thus, we conclude that the longitudinal variation derived for the D months is not a spurious feature caused by the sporadic occurrence of stratospheric sudden warming events. We also found that the elimination of PVW makes little difference in the phase of the semidiurnal lunar variation, and thus, the corresponding results are not shown in Figure 7.

Figure 10 compares the longitudinal dependence of the semidiurnal lunar variation derived from the (a–c) CHAMP-Swarm data with those obtained from version 2.0 of the (d–f) EEJM (CHAMP) and (g–i) EEJM (Ørsted). The results are shown only for the case that includes all solar times between 0800 and 1600 and all solar activity levels. The models reproduce well the longitudinal variation and its seasonal dependence. It should be noted, however, that the model-data agreement becomes poorer when comparisons are made for different binning cases (i.e., morning, afternoon, solar maximum, and solar minimum).

3.3. Wave Number Spectrum

A semidiurnal lunar tidal oscillation can be interpreted as a superposition of different modes with different wave numbers and may be expressed as follows (e.g., Paulino et al., 2013):

$$\sum_s A_s \cos\left(2\tau + (s-2)\,\lambda - \phi_s\right) \tag{2}$$

Here s is the zonal wave number, τ is lunar time, λ is longitude, A_s and ϕ_s are the amplitude and phase, respectively, $s < 0$ and $s > 0$ represent eastward and westward propagating waves, respectively, and $s = 0$ corresponds to a stationary tidal wave. The $s = 2$ mode represents the migrating tide, and all other $s \neq 2$ modes are nonmigrating tides. Paulino et al. (2013) identified several nonmigrating modes (SE1, SE2, SW5, and SW6) along with the dominant migrating mode (SW2) in the semidiurnal lunar tidal oscillation of the lower thermospheric temperature observed at 108 km during 2002–2012.

Figures 11a–11c shows the wave number spectra for the semidiurnal lunar variation of the equatorial electrojet. As expected, the dominant component is the migrating tide (SW2). There are smaller but persistent contributions from SW3 and SW4. It is interesting to note that the amplitudes of SW3 and SW4 do not show much seasonal variability, while the SW2 amplitude depends strongly on the season. Another interesting fact is that eastward propagating modes ($s < 0$) are largely missing from the spectra. This contrasts with solar tidal spectra of the equatorial electrojet, which show significant contributions from eastward propagating modes (Lühr & Manoj, 2013). In particular, the eastward propagating diurnal solar tide with wave number 3 (DE3) is known to be the main cause of the four-peak longitudinal pattern in the mean equatorial electrojet intensity from April to October (Lühr & Manoj, 2013; Lühr et al., 2008) (see also Figures 1 and 9). The DE3 solar tidal wave is generated by longitudinally inhomogeneous heating in the troposphere, which results from the surface topography and land-sea distribution (Hagan & Forbes, 2002; Zhang et al., 2006, 2010a, 2010b).

We present in Figures 11d–11e the reconstruction of the equatorial electrojet perturbations due to SW3 and SW4. The variation pattern is similar in different seasons, but the phase of the semidiurnal variation is shifted to earlier lunar times during the Northern Hemisphere winter compared to the Northern Hemisphere summer. Figures 11g–11i show the same as Figures 10a–10c except that the longitudinal average is subtracted at each lunar time to isolate nonmigrating components. The effect of SW3 and SW4 (Figures 11d–11e) explains the main features of the variation pattern seen in Figures 11g–11i. It is noted that the nonmigrating waves SW3 and SW4 can only explain the longitudinal structure with zonal wave number up to 2 (or the structure with the zonal wave length longer than 180°). Finer longitudinal structures seen in Figure 7 require consideration of other nonmigrating tidal modes, which are relatively small and thus will not be discussed further here.

It is important to note that the SW3 and SW4 spectra in Figures 11a–11c do not necessarily indicate the existence of nonmigrating lunar tides in the neutral atmosphere at dynamo region heights. These nonmigrating tidal modes did not show particularly large amplitudes in the results presented by Paulino et al. (2013)

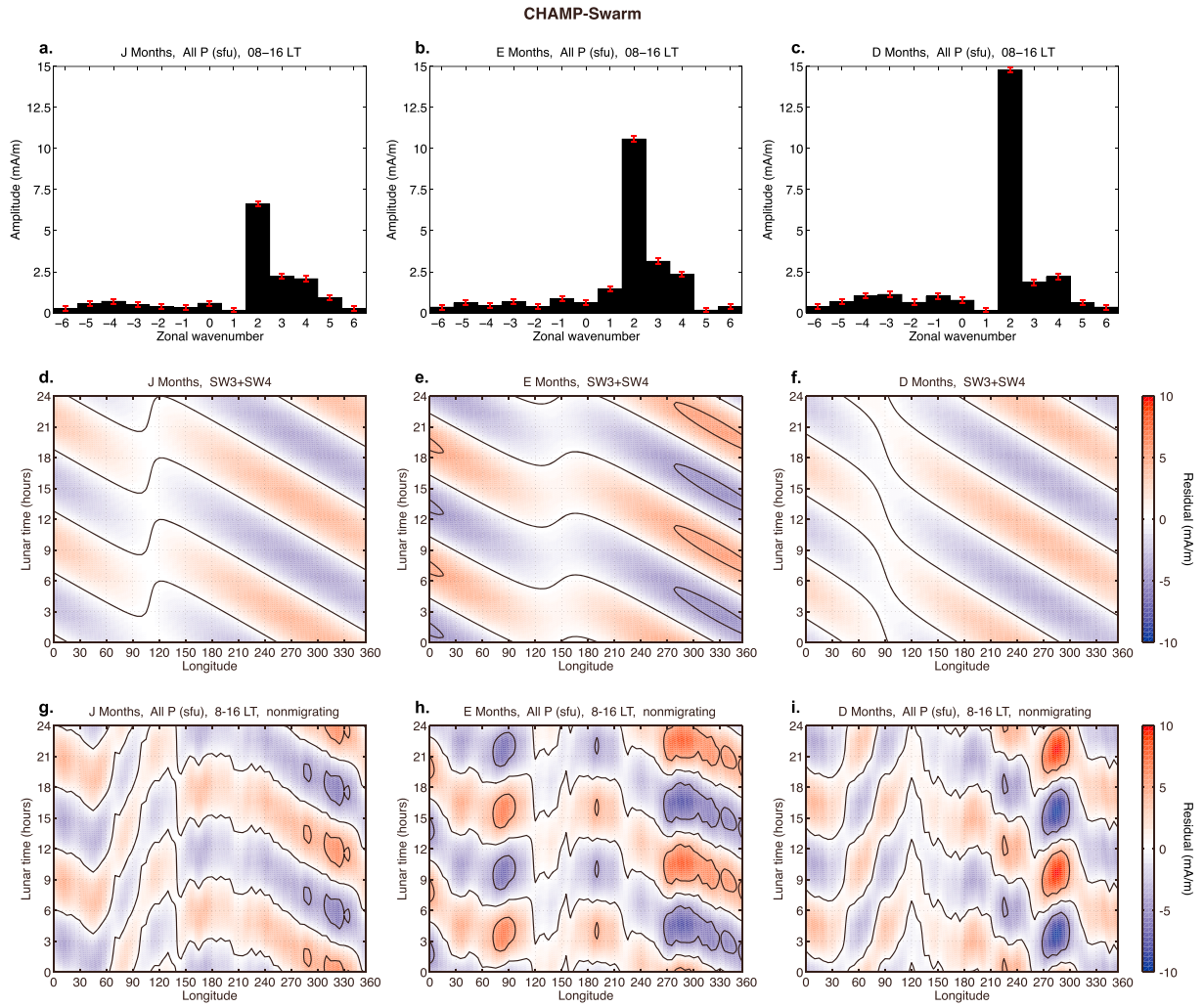

Figure 11. (a–c) Zonal wave number spectra of the semidiurnal lunar variation in the equatorial electrojet intensity for the (left column) J months, (middle column) E months, and (right column) D months. (d–f) Reconstruction of the lunar tidal perturbations in the equatorial electrojet intensity associated with SW3 and SW4. (g–i) Same as Figures 10a–10c except that the longitudinal average is subtracted at each lunar time.

for the lower thermospheric temperature during 2002–2012. As can be understood from equation (1), longitudinal variability of the equatorial electrojet can arise not only from the longitudinal variation of the neutral wind **U** but also from the longitudinal variation of the background geomagnetic field **B**. The latter modifies the ionospheric conductivity $\hat{\sigma}$ as well as the driving force $\mathbf{U} \times \mathbf{B}$. The inverse relationship between the lunar tidal amplitude and the background geomagnetic field strength observed during the equinoxes (Figure 8) indicates that the lunar current is longitudinally modulated because of the stationary zonal structure in the background geomagnetic field. The stationary zonal structure embedded in the ionosphere acts to broaden the wave number spectra. For instance, Yue et al. (2013) numerically demonstrated how the westward propagating quasi 2 day wave with zonal wave number 3 (W3) can produce quasi 2 day ionospheric oscillations with broader zonal wave number spectra (W1, W2, W4, W5, etc. besides W3). It is possible that SW3 and SW4 in the lunar tidal variation of the equatorial electrojet intensity is a result of migrating tidal forcing on the zonally inhomogeneous ionosphere.

3.4. Seasonal-Longitudinal Climatology

The complete seasonal-longitudinal climatology is depicted in Figure 12 using the data for all solar times between 0800 and 1600 and all solar activity levels. The seasonal and longitudinal variations were obtained by binning the data into 3-monthly 30° longitudinal bins. For each bin, the amplitude and phase were calculated, along with their 1 σ errors. The largest values of the error are indicated in Figure 12. The largest error

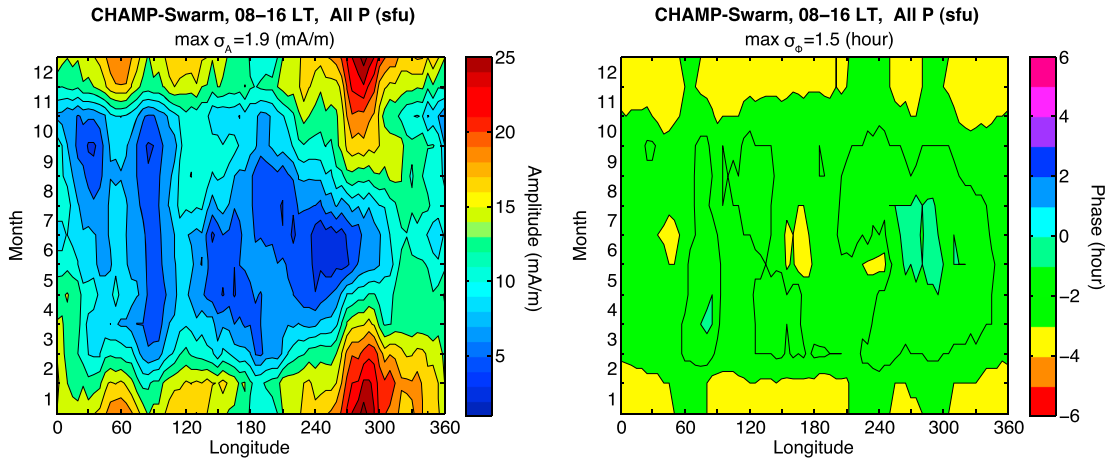

Figure 12. Seasonal and longitudinal dependence of the (left) amplitude and (right) phase of the semidiurnal lunar variation in the equatorial electrojet intensity.

in the amplitude occurred at 285°E in January (where the amplitude is large), while the largest error in the phase occurred at 245°E in July (where the amplitude is small).

The results shown in Figure 12 confirm the seasonal-longitudinal dependence of the semidiurnal lunar variation presented in Figure 7, which was derived with a slightly different binning method. The amplitude and phase are similar at the two equinoxes, which justifies the three seasonal binning used in earlier analyses.

Both amplitude and phase are subject to an annual variation. The amplitude tends to be greatest and the phase tends to be earliest during the Northern Hemisphere winter. These annual variations seem to be consistent with the seasonal variability of the lunar tide in the neutral atmosphere at dynamo region heights (Pedatella, 2014).

The amplitude peaks in the Peruvian sector (~285°E) from September to April. During May–August, the peak amplitude occurs in the Brazilian sector (~325°E). The large lunar tidal amplitude in the South American region can be understood, at least qualitatively, as the effect of enhanced ionospheric conductivities due to the weak background geomagnetic field. The strength of the background geomagnetic field over the magnetic equator minimizes at ~300°E (see Figure 1b). In addition, the magnetic equator is located in the Southern Hemisphere over the Peruvian region (Figure 1a), which implies that the ionization rate (and hence the ionospheric conductivity) is highest during the Northern Hemisphere winter. This could also contribute to the large lunar tidal variation in the Peruvian sector during the D months. In Figure 12, local amplitude maxima can also be seen at ~55°E and ~120°E throughout the year. The structure seems to be associated with the local reduction of ionospheric conductivities due to the strong background geomagnetic field at ~100°E.

4. Conclusions

We have studied the climatology of the semidiurnal lunar variation in the equatorial electrojet intensity using magnetic field measurements from the CHAMP and Swarm satellites. The complete seasonal-longitudinal dependence was revealed for the first time based on the global satellite data. The main results of the present study may be summarized as follows:

1. Significant longitudinal variability is found in the amplitude of the semidiurnal lunar variation, while the longitudinal variation in the phase is small (~1 h).
2. The longitudinal pattern of the amplitude depends on the season. The peak amplitude occurs at ~285°E during September–April and at ~325°E during May–August. There are also local amplitude maxima at ~55°E and ~120°E, which can be observed throughout the year.
3. The amplitude correlates well with the reciprocal of the background geomagnetic field strength during the equinoxes.
4. The amplitude does not correlate with the mean (background) equatorial electrojet intensity.
5. A tidal spectrum analysis reveals the dominance of the migrating mode SW2 with secondary contributions by the nonmigrating modes SW3 and SW4. The composition of nonmigrating modes is different from that in the neutral atmosphere reported by Paulino et al. (2013).

The observed longitudinal variation of the amplitude can be partly explained by the effect of ionospheric conductivities, which vary inversely with the strength of the background geomagnetic field. However, many aspects of the longitudinal variability cannot be understood simply by the distribution of the background geomagnetic field. More studies will be required to separate the contributions of ionospheric conductivities and nonmigrating lunar tides to the longitudinal dependence of the semidiurnal lunar variation in the equatorial electrojet. Accurate knowledge of the *E* region ionospheric conductivities and their longitudinal dependence will be necessary, as well as a better understanding of nonmigrating lunar tides.

Acknowledgments
The CHAMP satellite mission has been operated by GFZ Potsdam and DLR (former DARA). CHAMP data can be downloaded from http://isdc.gfz-potsdam.de/champ-isdc. The Swarm satellite constellation mission is operated by the European Space Agency (ESA). Swarm data are accessible through http://www.earth.esa.int/swarm. Versions 1.0 and 2.0 of the EEJM can be downloaded from the CIRES website at http://geomag.colorado.edu/equatorial-electrojet-model-eejm2.html. The geomagnetic activity index *Kp* was provided by the GFZ German Research Centre for Geosciences and available at http://www.gfz-potsdam.de/kp-index. The $F_{10.7}$ index was provided by the Natural Resources Canada, available at http://www.spaceweather.ca/solarflux/sx-en.php. C. S., J. M., T. A. S., and H. L. are partly supported by the Priority Program 1788 "Dynamic Earth" of the Deutsche Forschungsgemeinschaft (DFG).

References

Alken, P. (2009). Modeling equatorial ionospheric currents and electric fields from satellite magnetic field measurements (PhD thesis). Boulder, CO: University of Colorado Boulder.

Alken, P. (2016). Observations and modeling of the ionospheric gravity and diamagnetic current systems from CHAMP and Swarm measurements. *Journal of Geophysical Research: Space Physics*, *121*, 589–601. https://doi.org/10.1002/2015JA022163

Alken, P., Chulliat, A., & Maus, S. (2013). Longitudinal and seasonal structure of the ionospheric equatorial electric field. *Journal of Geophysical Research: Space Physics*, *118*, 1298–1305. https://doi.org/10.1029/2012JA018314

Alken, P., & Maus, S. (2007). Spatio-temporal characterization of the equatorial electrojet from CHAMP, Ørsted, and SAC-C satellite magnetic measurements. *Journal of Geophysical Research*, *112*, A09305. https://doi.org/10.1029/2007JA012524

Alken, P., Maus, S., Chulliat, A., Vigneron, P., Sirol, O., & Hulot, G. (2015). Swarm equatorial electric field chain: First results. *Geophysical Research Letters*, *42*, 673–680. https://doi.org/10.1002/2014GL062658

Alken, P., Maus, S., Richmond, A. D., & Maute, A. (2011). The ionospheric gravity and diamagnetic current systems. *Journal of Geophysical Research*, *116*, A12316. https://doi.org/10.1029/2011JA017126

Alken, P., Maus, S., Vigneron, P., Sirol, O., & Hulot, G. (2013). Swarm SCARF equatorial electric field inversion chain. *Earth Planets Space*, *65*(11), 1309–1317. https://doi.org/10.5047/eps.2013.09.008

Andrews, D., Holton, J. R., & Leovy, C. B. (1987). *Middle atmosphere dynamics* (pp. 259–294). New York: Elsevier.

Aso, T., Nonoyama, T., & Kato, S. (1981). Numerical simulation of semidiurnal atmospheric tides. *Journal of Geophysical Research*, *86*(A13), 11388–11400. https://doi.org/10.1029/JA086iA13p11388

Balan, N., & Iyer, K. N. (1983). Equatorial anomaly in ionospheric electron content and its relation to dynamo currents. *Journal of Geophysical Research*, *88*, 10,259–10,262.

Baker, W. G., & Martyn, D. F. (1953). Electric currents in the ionosphere. I. The conductivity. *Philosophical Transactions of the Royal Society of London, Series A*, *246*, 281–294.

Bartels, J., & Johnston, H. F. (1940). Geomagnetic tides in horizontal intensity at Huancayo, Part I. *Terrestrial Magnetism and Atmospheric Electricity*, *45*(3), 269–308. https://doi.org/10.1029/TE045i003p00269

Bhuyan, P., & Tyagi, T. (1986). Lunar and solar daily variations of ionospheric electron content at Delhi. *Journal of Atmospheric and Terrestrial Physics*, *48*(3), 301–310. https://doi.org/10.1016/0021-9169(86)90106-6

Çelik, C. (2014). The lunar daily geomagnetic variation and its dependence on sunspot number. *Journal of Atmospheric and Solar-Terrestrial Physics*, *119*, 153–161.

Chau, J. L., Hoffmann, P., Pedatella, N. M., Matthias, V., & Stober, G. (2015). Upper mesospheric lunar tides over middle and high latitudes during sudden stratospheric warming events. *Journal of Geophysical Research: Space Physics*, *120*, 3084–3096. https://doi.org/10.1002/2015JA020998

Chulliat, A., Vigneron, P., & Hulot, G. (2016). First results from the Swarm dedicated ionospheric field inversion chain. *Earth Planets Space*, *68*, 104. https://doi.org/10.1186/s40623-016-0481-6

Cnossen, I. (2017). The impact of century-scale changes in the core magnetic field on external magnetic field contributions. *Space Science Reviews*, *206*, 259–280. https://doi.org/10.1007/s11214-016-0276-x

Cnossen, I., Richmond, A. D., & Wiltberger, M. (2012). The dependence of the coupled magnetosphere-ionosphere-thermosphere system on the Earth's magnetic dipole moment. *Journal of Geophysical Research*, *117*, A05302. https://doi.org/10.1029/2012JA017555

Dee, D. P., Uppala, S. M., Simmons, A. J., Berrisford, P., Poli, P., Kobayashi, S., … Vitart, F. (2011). The ERA-Interim reanalysis: Configuration and performance of the data assimilation system. *Quarterly Journal of the Royal Meteorological Society*, *137*, 553–597.

Doumouya, V., Cohen, Y., Arora, B. R., & Yumoto, K. (2003). Local time and longitude dependence of the equatorial electrojet magnetic effects. *Journal of Atmospheric and Solar-Terrestrial Physics*, *65*, 1265–1282.

Dunford, E. (1967). The relationship between the ionospheric equatorial anomaly and the *E*-region current system. *Journal of Atmospheric and Terrestrial Physics*, *29*, 1489–1498.

Eccles, V., Rice, D. D., Sojka, J. J., Valladares, C. E., Bullett, T., & Chau, J. L. (2011). Lunar atmospheric tidal effects in the plasma drifts observed by the low-latitude ionospheric sensor network. *Journal of Geophysical Research*, *116*, A07309. https://doi.org/10.1029/2010JA016282

Efron, B. (1981). Nonparametric estimates of standard error: The jackknife, the bootstrap, and other methods. *Biometrika*, *68*(3), 589–599.

England, S. L., Maus, S., Immel, T. J., & Mende, S. B. (2006). Longitudinal variation of the *E* region electric fields caused by atmospheric tides. *Geophysical Research Letters*, *33*, L21105. https://doi.org/10.1029/2006GL027465

Fang, T.-W., Kil, H., Millward, G., Richmond, A. D., Liu, J.-Y., & Oh, S.-J. (2009). Causal link of the wave-4 structures in plasma density and vertical plasma drift in the low-latitude ionosphere. *Journal of Geophysical Research*, *114*, A10315. https://doi.org/10.1029/2009JA014460

Fejer, B. G., & Tracy, B. D. (2013). Lunar tidal effects in the electrodynamics of the low latitude ionosphere. *Journal of Atmospheric and Solar-Terrestrial Physics*, *103*, 76–82.

Fejer, B., Farley, D., Woodman, R., & Calderon, C. (1979). Dependence of equatorial *F* region vertical drifts on season and solar cycle. *Journal of Geophysical Research*, *84*(A10), 5792–5796. https://doi.org/10.1029/JA084iA10p05792

Fejer, B. G., Jensen, J. W., & Su, S.-Y. (2008). Quiet time equatorial *F* region vertical plasma drift model derived from ROCSAT-1 observations. *Journal of Geophysical Research*, *113*, A05304. https://doi.org/10.1029/2007JA012801

Fejer, B. G., Olson, M. E., Chau, J. L., Stolle, C., Lühr, H., Goncharenko, L. P., … Nagatsuma, T. (2010). Lunar dependent equatorial ionospheric electrodynamic effects during sudden stratospheric warmings. *Journal of Geophysical Research*, *115*, A00G03. https://doi.org/10.1029/2010JA015273

Forbes, J. M. (1982a). Atmospheric tides: 2. The solar and lunar semi-diurnal components. *Journal of Geophysical Research*, *87*(A7), 5241–5252. https://doi.org/10.1029/JA087iA07p05241

Forbes, J. M. (1982b). Atmospheric tides: 1. Model description and results for the solar diurnal component. *Journal of Geophysical Research*, *87*(A7), 5222–5240. https://doi.org/10.1029/JA087iA07p05222

Forbes, J. M., & Lindzen, R. S. (1976). Atmospheric solar tides and their electrodynamic effects—I. The global S_q current system. *Journal of Atmospheric and Terrestrial Physics*, *38*, 897–910.

Forbes, J. M., & Zhang, X. (2012). Lunar tide amplification during the January 2009 stratosphere warming event: Observations and theory. *Journal of Geophysical Research*, *117*, A12312. https://doi.org/10.1029/2012JA017963

Forbes, J. M., Zhang, X., Bruinsma, S., & Oberheide, J. (2013). Lunar semidiurnal tide in the thermosphere under solar minimum conditions. *Journal of Geophysical Research: Space Physics*, *118*, 1788–1801. https://doi.org/10.1029/2012JA017962

Forbes, J. M., Zhang, X., Palo, S., Russell, J., Mertens, C. J., & Mlynczak, M. (2008). Tidal variability in the ionospheric dynamo region. *Journal of Geophysical Research*, *113*, A02310. https://doi.org/10.1029/2007JA012737

Friis-Christensen, E., Lühr, H., & Hulot, G. (2006). Swarm: A constellation to study the Earth's magnetic field. *Earth Planets Space*, *58*, 351–358.

Friis-Christensen, E., Lühr, H., Knudsen, D., & Haagmans, R. (2008). Swarm—An Earth observation mission investigating geospace. *Advances in Space Research*, *41*, 210–216. https://doi.org/10.1016/j.asr.2006.10.008

Glassmeier, K. H., Vogt, J., Stadelmann, A., & Buchert, S. (2004). Concerning long-term geomagnetic variations and space climatology. *Annales Geophysicae*, *22*(10), 3669–3677.

Gupta, J. C. (1973). On solar and lunar equatorial electrojets. *Annales Geophysicae*, *29*(1), 49–60.

Hagan, M. E., & Forbes, J. M. (2002). Migrating and nonmigrating diurnal tides in the middle and upper atmosphere excited by tropospheric latent heat release. *Journal of Geophysical Research*, *107*(D24), 4754. https://doi.org/10.1029/2001JD001236

Hagan, M. E., Roble, R. G., & Hackney, J. (2001). Migrating thermospheric tides. *Journal of Geophysical Research*, *106*(A7), 12,739–12,752. https://doi.org/10.1029/2000JA000344

Hanson, W. B., & Moffett, R. J. (1966). Ionization transport effects in the equatorial *F* region. *Journal of Geophysical Research*, *71*(23), 5559–5572. https://doi.org/10.1029/JZ071i023p05559

Hirono, M. (1950). On the influence of the Hall current to the electrical conductivity of the ionosphere. I. *Journal of Geomagnetism and Geoelectricity*, *2*, 1–8.

Hysell, D. L., Chau, J. L., & Fesen, C. G. (2002). Effects of large horizontal winds on the equatorial electrojet. *Journal of Geophysical Research*, *107*(A8), SIA 27-1–SIA 27-12, 1214. https://doi.org/10.1029/2001JA000217

Jin, H., Miyoshi, Y., Fujiwara, H., & Shinagawa, H. (2008). Electrodynamics of the formation of ionospheric wave number 4 longitudinal structure. *Journal of Geophysical Research*, *113*, A09307. https://doi.org/10.1029/2008JA013301

Kawano-Sasaki, K., & Miyahara, S. (2008). A study on three-dimensional structures of the ionospheric dynamo currents induced by the neutral winds simulated by the Kyushu-GCM. *Journal of Atmospheric and Solar-Terrestrial Physics*, *70*, 1549–1562.

Labitzke, K., & van Loon, H. (1999). *The stratosphere: Phenomena, history, and relevance*. New York: Springer.

Le Mouël, J. L., Shebalin, P., & Chulliat, A. (2006). The field of the equatorial electrojet from CHAMP data. *Annales Geophysicae*, *24*, 515–527.

Lieberman, R. S., Fritts, D. C., Pedatella, N., Doornbos, E., & Ortland, D. A. (2015). Global observations of thermospheric lunar tidal winds. *Journal of Atmospheric and Solar-Terrestrial Physics*, *136*, 126–133.

Lindzen, R. S., & Chapman, S. (1969). Atmospheric tides. *Space Science Reviews*, *10*, 3–188.

Lindzen, R. S., & Hong, S. S. (1974). Effects of mean winds and horizontal temperature gradients on solar and lunar semidiurnal tides in the atmosphere. *Journal of Atmospheric Sciences*, *31*, 1421–1466.

Lühr, H., Kervalishvili, G., Michaelis, I., Rauberg, J., Ritter, P., Park, J., … Brauer, P. (2015). The interhemispheric and *F* region dynamo currents revisited with the Swarm constellation. *Geophysical Research Letters*, *42*, 3069–3075. https://doi.org/10.1002/2015GL063662

Lühr, H., & Manoj, C. (2013). The complete spectrum of the equatorial electrojet related to solar tides: CHAMP observations. *Annales Geophysicae*, *31*, 1315–1331. https://doi.org/10.5194/angeo-31-1315-2013

Lühr, H., & Maus, S. (2006). Direct observation of the *F* region dynamo currents and the spatial structure of the EEJ by CHAMP. *Geophysical Research Letters*, *33*, L24102. https://doi.org/10.1029/2006GL028374

Lühr, H., Maus, S., & Rother, M. (2004). Noon-time equatorial electrojet: Its spatial features as determined by the CHAMP satellite. *Journal of Geophysical Research*, *109*, A01306. https://doi.org/10.1029/2002JA009656

Lühr, H., Rother, M., Häusler, K., Alken, P., & Maus, S. (2008). The influence of nonmigrating tides on the longitudinal variation of the equatorial electrojet. *Journal of Geophysical Research*, *113*, A08313. https://doi.org/10.1029/2008JA013064

Lühr, H., Siddiqui, T. A., & Maus, S. (2012). Global characteristics of the lunar tidal modulation of the equatorial electrojet derived from CHAMP observations. *Annales Geophysicae*, *30*(3), 527–536. https://doi.org/10.5194/angeo-30-527-2012

Maeda, H., & Fujiwara, M. (1967). Lunar ionospheric winds deduced from the dynamo theory of geomagnetic variations. *Journal of Atmospheric and Terrestrial Physics*, *29*, 917–936.

Malin, S. R. C. (1973). Worldwide distribution of geomagnetic tides. *Philosophical Transactions of the Royal Society of London, Series A*, *274*, 551–594.

Manoj, C., Lühr, H., Maus, S., & Nagarajan, N. (2006). Evidence for short spatial correlation lengths of the noontime equatorial electrojet inferred from a comparison of satellite and ground magnetic data. *Journal of Geophysical Research*, *111*, A11312. https://doi.org/10.1029/2006JA011855

Matsushita, S. (1967). Lunar tides in the ionosphere. *Handbook of Physics*, *49*(2), 547–602.

Matsushita, S. (1969). Dynamo currents, winds, and electric fields. *Radio Science*, *4*(9), 771–780. https://doi.org/10.1029/RS004i009p00771

Matsushita, S., & Xu, W.-Y. (1984). Seasonal variations of L equivalent current systems. *Journal of Geophysical Research*, *89*(A1), 285–294.

Matzka, J., Siddiqui, T. A., Lilienkamp, H., Stolle, C., & Veliz, O. (2017). Quantifying solar flux and geomagnetic main field influence on the equatorial ionospheric current system at the geomagnetic observatory Huancayo. *Journal of Atmospheric and Solar-Terrestrial Physics*, *163*, 120–125. https://doi.org/https://doi.org/10.1016/j.jastp.2017.04.014

Maus, S., & Lühr, H. (2006). A gravity-driven electric current in the Earth's ionosphere identified in CHAMP satellite magnetic measurements. *Geophysical Research Letters*, *33*, L02812. https://doi.org/10.1029/2005GL024436

Maute, A., Fejer, B. G., Forbes, J. M., Zhang, X., & Yudin, V. (2016). Equatorial vertical drift modulation by the lunar and solar semidiurnal tides during the 2013 sudden stratospheric warming. *Journal of Geophysical Research: Space Physics*, *121*, 1658–1668. https://doi.org/10.1002/2015JA022056

Miyahara, S., & Ooishi, M. (1997). Variation of Sq induced by atmospheric tides simulated by a middle atmosphere general circulation model. *Journal of Geomagnetism and Geoelectricity*, *49*, 77–87.

Moffett, R. J., & Hanson, W. B. (1965). Effect of ionization transport on the equatorial *F*-region. *Nature*, *206*(4985), 705–706. https://doi.org/10.1038/206705a0

Niu, X., Xiong, J., Wan, W., Ning, B., Liu, L., Vincent, R. A., & Reid, I. M. (2005). Lunar tidal winds in the mesosphere over Wuhan and Adelaide. *Advances in Space Research*, *36*, 2218–2222.

Niu, X. J., Xiong, J. G., Wan, W. X., Ning, B. Q., & Liu, L. B. (2007). A measurement of the lunar semidiurnal tide at Wuhan (30°40′N, 114°30′E). *Earth Planets Space*, *59*, 991–997.
Oberheide, J., Forbes, J. M., Zhang, X., & Bruinsma, S. L. (2011). Climatology of upward propagating diurnal and semidiurnal tides in the thermosphere. *Journal of Geophysical Research*, *116*, A11306. https://doi.org/10.1029/2011JA016784
Onwumechilli, C. A., & Alexander, N. S. (1959). Variations in the geomagnetic field at Ibadan, Nigeria, II: Lunar and luni-solar variations in H and Z. *Journal of Atmospheric and Terrestrial Physics*, *16*, 115–123.
Park, J., Lühr, H., Kunze, M., Fejer, B. G., & Min, K. W. (2012). Effect of sudden stratospheric warming on lunar tidal modulation of the equatorial electrojet. *117*, A03306. https://doi.org/10.1029/2011JA017351
Park, J., Lühr, H., & Min, K. W. (2011). Climatology of the inter-hemispheric field-aligned current system in the equatorial ionosphere as observed by CHAMP. *Annales Geophysicae*, *29*, 573–582. https://doi.org/10.5194/angeo-29-573-2011
Paulino, A. R., Batista, P. P., & Batista, I. S. (2013). A global view of the atmospheric lunar semidiurnal tide. *Journal of Geophysical Research: Atmospheres*, *118*, 13128–13139. https://doi.org/10.1002/2013JD019818
Paulino, A. R., Batista, P. P., & Clemesha, R. (2012). Lunar tides in the mesosphere and lower thermosphere over Cachoeira Paulista (22.7°S; 45.0°W). *Journal of Atmospheric and Solar-Terrestrial Physics*, *78–79*, 31–36.
Paulino, A. R., Batista, P. P., Lima, L. M., Clemesha, R., Buriti, R. A., & Schuch, N. (2015). The lunar tides in the mesosphere and lower thermosphere over Brazilian sector. *Journal of Atmospheric and Solar-Terrestrial Physics*, *133*, 129–138.
Paulino, A. R., Lima, L. M., Almeida, S. L., Batista, P. P., Batista, I. S., & Paulino, I. (2017). Lunar tides in total electron content over Brazil. *Journal of Geophysical Research: Space Physics*, *122*, 7519–7529. https://doi.org/10.1002/2017JA024052
Pedatella, N. M. (2014). Observations and simulations of the ionospheric lunar tide: Seasonal variability. *Journal of Geophysical Research: Space Physics*, *119*, 5800–5806. https://doi.org/10.1002/2014JA020189
Pedatella, N. M., & Forbes, J. M. (2010). Global structure of the lunar tide in ionospheric total electron content. *Geophysical Research Letters*, *37*, L06103. https://doi.org/10.1029/2010GL042781
Pedatella, N. M., Forbes, J. M., & Richmond, A. D. (2011). Seasonal and longitudinal variations of the solar quiet (*Sq*) current system during solar minimum determined by CHAMP satellite magnetic field observations. *Journal of Geophysical Research*, *116*, A04317. https://doi.org/10.1029/2010JA016289
Pedatella, N. M., Hagan, M. E., & Maute, A. (2012). The comparative importance of DE3, SE2, and SPW4 on the generation of wavenumber-4 longitude structures in the low-latitude ionosphere during September equinox. *Geophysical Research Letters*, *39*, L19108. https://doi.org/10.1029/2012GL053643
Pedatella, N. M., & Liu, H.-L. (2013). The influence of atmospheric tide and planetary wave variability during sudden stratosphere warmings on the low latitude ionosphere. *Journal of Geophysical Research: Space Physics*, *118*, 5333–5347. https://doi.org/10.1002/jgra.50492
Pedatella, N. M., Liu, H.-L., & Richmond, A. D. (2012). Atmospheric semidiurnal lunar tide climatology simulated by the Whole Atmosphere Community Climate Model. *Journal of Geophysical Research*, *117*, A06327. https://doi.org/10.1029/2012JA017792
Pedatella, N. M., Liu, H.-L., Richmond, A. D., Maute, A., & Fang, T.-W. (2012). Simulations of solar and lunar tidal variability in the mesosphere and lower thermosphere during sudden stratosphere warmings and their influence on the low-latitude ionosphere. *Journal of Geophysical Research*, *117*, A08326. https://doi.org/10.1029/2012JA017858
Pedatella, N. M., Liu, H.-L., Sassi, F., Lei, J., Chau, J. L., & Zhang, X. (2014). Ionosphere variability during the 2009 SSW: Influence of the lunar semidiurnal tide and mechanisms producing electron density variability. *Journal of Geophysical Research: Space Physics*, *119*, 3828–3843. https://doi.org/10.1002/2014JA019849
Raja Rao, K. S., & Sivaraman, K. R. (1958). Lunar geomagnetic tides at Kodaikanal. *Journal of Geophysical Research*, *63*(4), 727–730. https://doi.org/10.1029/JZ063i004p00727
Rastogi, R. G. (1962). Longitudinal variation in the equatorial electrojet. *Journal of Atmospheric and Terrestrial Physics*, *24*, 1031–1040.
Rastogi, R. G., Chandra, H., & Sethia, G. (1985). Solar and lunar variations in TEC at low latitudes in India. *Journal of Atmospheric and Terrestrial Physics*, *47*(4), 309–317.
Rastogi, R. G., & Klobuchar, J. A. (1990). Ionospheric electron content within the equatorial F_2 layer anomaly belt. *Journal of Geophysical Research*, *95*(A11), 19,045–19,052. https://doi.org/10.1029/JA095iA11p19045
Rastogi, R. G., & Trivedi, N. B. (1970). Luni-solar tides in H at stations within the equatorial electrojet. *Planetary and Space Science*, *18*(3), 367–377.
Reigber, C., Lühr, H., & Schwintzer, P. (2002). CHAMP mission status. *Advances in Space Research*, *30*, 129–134.
Richards, P. G., Fennelly, J. A., & Torr, D. G. (1994). EUVAC: A solar EUV flux model for aeronomic calculations. *Journal of Geophysical Research*, *99*(A5), 8981–8992. https://doi.org/10.1029/94JA00518
Richmond, A. D. (1973). Equatorial electrojet—I. Development of a model including winds and instabilities. *Journal of Atmospheric and Terrestrial Physics*, *35*, 1083–1103.
Richmond, A. D. (1979). Ionospheric wind dynamo theory: A review. *Journal of Geomagnetism and Geoelectricity*, *31*, 287–310.
Richmond, A. D. (1989). Modeling the ionosphere wind dynamo: A review. *Pure and Applied Geophysics*, *47*, 413–435.
Richmond, A. D. (1995). Ionospheric electrodynamics. In H. Volland (Ed.), *Handbook of Atmospheric Electrodynamics* (Vol. 2, pp. 249–290). Boca Raton, FL: CRC Press.
Richmond, A. D., Matsushita, S., & Tarpley, J. D. (1976). On the production mechanism of electric currents and fields in the ionosphere. *Journal of Geophysical Research*, *81*(4), 547–555.
Richmond, A. D., & Roble, R. G. (1987). Electrodynamic effects of the thermospheric winds from the NCAR thermospheric general circulation model. *Journal of Geophysical Research*, *92*(A11), 12,365–12,376.
Rush, C. M., & Richmond, A. D. (1973). The relationship between the structure of the equatorial anomaly and the strength of the equatorial electrojet. *Journal of Atmospheric and Terrestrial Physics*, *35*, 1171–1180.
Sandford, D. J., Muller, H. G., & Mitchell, N. J. (2006). Observations of lunar tides in the mesosphere and lower thermosphere at Arctic and middle latitudes. *Atmospheric Chemistry and Physics*, *6*, 4117–4127.
Sathishkumar, S., Sridharan, S., Muhammed Kutty, P. V., & Gurubaran, S. (2017). Long term variabilities and tendencies of mesospheric lunar semidiurnal tide over Tirunelveli (8.7°N, 77.8°). *Journal of Atmospheric and Solar-Terrestrial Physics*, *119*, 5800–5806.
Siddiqui, T. A., Lühr, H., Stolle, C., & Park, J. (2015). Relation between stratospheric sudden warming and the lunar effect on the equatorial electrojet based on Huancayo recordings. *Annales Geophysicae*, *33*(2), 235–243. https://doi.org/10.5194/angeo-33-235-2015
Siddiqui, T. A., Stolle, C., & Lühr, H. (2017). Longitude-dependent lunar tidal modulation of the equatorial electrojet during stratospheric sudden warmings. *Journal of Geophysical Research: Space Physics*, *122*, 3760–3776. https://doi.org/10.1002/2016JA023609
Siddiqui, T. A., Stolle, C., Luhr, H., & Matzka, J. (2015). On the relationship between weakening of the northern polar vortex and the lunar tidal amplification in the equatorial electrojet. *Journal of Geophysical Research: Atmosphere*, *120*, 5800–5806. https://doi.org/10.1002/2015JA021683

Stening, R. J. (1969). An assessment of the contributions of various tidal winds to the S_q current system. *Planetary and Space Science*, *17*, 889–908.
Stening, R. J. (1995). What drives the equatorial electrojet? *Journal of Atmospheric and Solar-Terrestrial Physics*, *57*, 1117–1128.
Stening, R. J. (2003). Space weather in the equatorial ionosphere. *Space Science Reviews*, *107*, 263–271.
Stening, R. J. (2011). Lunar tide in the equatorial electrojet in relation to stratospheric warmings. *Journal of Geophysical Research*, *116*, A12315. https://doi.org/10.1029/2011JA017047
Stening, R. J., & Fejer, B. G. (2001). Lunar tide in the equatorial *F* region vertical ion drift velocity. *Journal of Geophysical Research*, *106*(A1), 221–226. https://doi.org/10.1029/2000JA000175
Stening, R. J., & Jacobi, C. (2001). Lunar tidal winds in the upper atmosphere over Collm. *Annales Geophysicae*, *18*, 1645–1650.
Stening, R. J., & Vincent, R. A. (1989). A measurement of lunar tides in the mesosphere at Adelaide. *Journal of Geophysical Research*, *94*, 10,121–10,129.
Stening, R. J., Avery, S. K., & Tetenbaum, D. (1990). Observations of lunar tides in upper atmosphere winds at Poker Flat, Alaska. *Journal of Atmospheric and Terrestrial Physics*, *52*, 715–721.
Stening, R. J., Forbes, J. M., Hagan, M. E., & Richmond, A. D. (1997). Experiments with a lunar atmospheric tidal model. *Journal of Geophysical Research*, *102*(D12), 13,465–13,471. https://doi.org/10.1029/97JD00778
Stening, R. J., Meek, C. E., & Manson, A. H. (1987). Lunar tidal winds measured in the upper atmosphere (68–105 km) at Saskatoon, Canada. *Journal of Atmospheric Sciences*, *44*, 1143–1151.
Stening, R. J., Manson, A. H., Meek, C. E., & Vincent, R. A. (1994). Lunar tidal winds at Adelaide and Saskatoon at 80 to 100 km heights, 1985–1990. *Journal of Geophysical Research*, *99*, 13,273–13,280.
Stening, R. J., Schlapp, D. M., & Vincent, R. A. (1997). Lunar tides in the mesosphere over Christmas Island (2°N, 203°E). *Journal of Geophysical Research*, *102*(D22), 26,239–26,245. https://doi.org/10.1029/97JD00898
Stening, R. J., Richmond, A. D., & Roble, R. G. (1999). Lunar tides in the thermosphere-ionosphere-electrodynamics general circulation model. *Journal of Geophysical Research*, *104*(A1), 1–13. https://doi.org/10.1029/98JA02663
Stening, R. J., Tsuda, T., & Nakamura, T. (2003). Lunar tidal winds in the upper atmosphere over Jakarta. *Journal of Geophysical Research*, *108*, 1192. https://doi.org/10.1029/2002JA009528
Stolle, C., Manoj, C., Lühr, H., Maus, S., & Alken, P. (2008). Estimating the daytime equatorial ionization anomaly strength from electric field proxies. *Journal of Geophysical Research*, *113*, A09310. https://doi.org/10.1029/2007JA012781
Takeda, M. (1996). Effects of the strength of the geomagnetic main field strength on the dynamo action in the ionosphere. *Journal of Geophysical Research*, *101*(A4), 7875–7880. https://doi.org/10.1029/95JA03807
Takeda, M. (1999). Time variation of global geomagnetic Sq field in 1964 and 1980. *Journal of Atmospheric and Solar-Terrestrial Physics*, *61*, 765–774.
Takeda, M. (2013). Contribution of wind, conductivity, and geomagnetic main field to the variation in the geomagnetic Sq field. *Journal of Geophysical Research: Space Physics*, *118*, 4516–4522. https://doi.org/10.1002/jgra.50386
Takeda, M., & Maeda, H. (1980). Three-dimensional structure of ionospheric currents 1. Currents caused by diurnal tidal winds. *Journal of Geophysical Research*, *85*(A12), 6895–6899. https://doi.org/10.1029/JA085iA12p06895
Takeda, M., & Maeda, H. (1981). Three-dimensional structure of ionospheric currents 2. Currents caused by semidiurnal tidal winds. *Journal of Geophysical Research*, *86*(A7), 5861–5867. https://doi.org/10.1029/JA086iA07p05861
Takeda, M., Iyemori, T., & Saito, A. (2003). Relationship between electric field and currents in the ionosphere and the geomagnetic Sq field. *Journal of Geophysical Research*, *108*, 1183. https://doi.org/10.1029/2002JA009659
Tapping, K. F. (2013). The 10.7 cm solar radio flux ($F_{10.7}$). *Space Weather*, *11*, 394–406. https://doi.org/10.1002/swe.20064
Tarpley, J. D. (1970a). The ionospheric wind dynamo—II: Solar tides. *Planetary and Space Science*, *18*, 1091–1103.
Tarpley, J. D. (1970b). The ionospheric wind dynamo—I: Lunar tide. *Planetary and Space Science*, *18*, 1075–1090.
Tarpley, J. D., & Balsley, B. B. (1972). Lunar variations in the Peruvian electrojet. *Journal of Geophysical Research*, *77*(10), 1951–1960. https://doi.org/10.1029/JA077i010p01951
Tsuda, T., Tanii, J., Aso, T., & Kato, S. (1981). Lunar tides at meteor heights. *Geophysical Research Letters*, *8*(3), 191–194. https://doi.org/10.1029/GL008i003p00191
Uppala, S. M., Kållberg, P. W., Simmons, A. J., Andrae, U., Da Costa Bechtold, V., Fiorino, M., … Woollen, J. (2005). The ERA-40 re-analysis. *Quarterly Journal of the Royal Meteorological Society*, *131*, 2961–3012.
Vial, F., & Forbes, J. M. (1994). Monthly simulations of the lunar semidiurnal tide. *Journal of Atmospheric and Terrestrial Physics*, *56*, 1591–1607.
Yamazaki, Y. (2013). Large lunar tidal effects in the equatorial electrojet during northern winter and its relation to stratospheric sudden warming events. *Journal of Geophysical Research: Space Physics*, *118*, 7268–7271. https://doi.org/10.1002/2013JA019215
Yamazaki, Y., & Maute, A. (2017). Sq and EEJ—A review on the daily variation of the geomagnetic field caused by ionospheric dynamo currents. *Space Science Reviews*, *206*, 299–405. https://doi.org/10.1007/s11214-016-0282-z
Yamazaki, Y., Richmond, A. D., & Yumoto, K. (2012). Stratospheric warmings and the geomagnetic lunar tide: 1958–2007. *Journal of Geophysical Research*, *117*, A04301. https://doi.org/10.1029/2012JA017514
Yamazaki, Y., Yumoto, K., Cardinal, M. G., Fraser, B. J., Hattori, P., Kakinami, Y., … Yoshikawa, A. (2011). An empirical model of the quiet daily geomagnetic field variation. *Journal of Geophysical Research*, *116*, A10312. https://doi.org/10.1029/2011JA016487
Yamazaki, Y., Yumoto, K., McNamara, D., Hirooka, T., Uozumi, T., Kitamura, K., … Ikeda, A. (2012). Ionospheric current system during sudden stratospheric warming events. *Journal of Geophysical Research*, *117*, A03334. https://doi.org/10.1029/2011JA017453
Yamazaki, Y., Richmond, A. D., Maute, A., Wu, Q., Ortland, D. A., Yoshikawa, A., … Tsugawa, T. (2014). Ground magnetic effects of the equatorial electrojet simulated by the TIE-GCM driven by TIMED satellite data. *Journal of Geophysical Research: Space Physics*, *119*, 3150–3161. https://doi.org/10.1002/2013JA019487
Yamazaki, Y., Richmond, A. D., Maute, A., Liu, H.-L., Pedatella, N., & Sassi, F. (2014). On the day-to-day variation of the equatorial electrojet during quiet periods. *Journal of Geophysical Research: Space Physics*, *119*, 6966–6980. https://doi.org/10.1002/2014JA020243
Yamazaki, Y., Kosch, M. J., & Emmert, J. T. (2015). Evidence for stratospheric sudden warming effects on the upper thermosphere derived from satellite orbital decay data during 1967–2013. *Geophysical Research Letters*, *42*, 6180–6188. https://doi.org/10.1002/2015GL065395
Yiğit, E., & Medvedev, A. S. (2015). Internal wave coupling processes in Earth's atmosphere. *Advances in Space Research*, *55*, 983–1003.
Yizengaw, E., & Carter, B. A. (2017). Longitudinal, seasonal and solar cycle variation in lunar tide influence on the equatorial electrojet. *Annales Geophysicae*, *35*, 525–533. https://doi.org/10.5194/angeo-35-525-2017
Yue, J., Wang, W., Richmond, A. D., Liu, H.-L., & Chang, L. C. (2013). Wavenumber broadening of the quasi 2 day planetary wave in the ionosphere. *Journal of Geophysical Research: Space Physics*, *118*, 3515–3526. https://doi.org/10.1002/jgra.50307

Zhang, J. T., & Forbes, J. M. (2013). Lunar tidal winds between 80 and 110 km from UARS/HRDI wind measurements. *Journal of Geophysical Research: Space Physics*, *118*, 5296–5304. https://doi.org/10.1002/jgra.50420

Zhang, X., & Forbes, J. M. (2014). Lunar tide in the thermosphere and weakening of the northern polar vortex. *Geophysical Research Letters*, *41*, 8201–8207. https://doi.org/10.1002/2014GL062103

Zhang, X., Forbes, J. M., & Hagan, M. E. (2010a). Longitudinal variation of tides in the MLT region: 1. Tides driven by tropospheric net radiative heating. *Journal of Geophysical Research*, *115*, A06316. https://doi.org/10.1029/2009JA014897

Zhang, X., Forbes, J. M., & Hagan, M. E. (2010b). Longitudinal variation of tides in the MLT region: 2. Relative effects of solar radiative and latent heating. *Journal of Geophysical Research*, *115*, A06317. https://doi.org/10.1029/2009JA014898

Zhang, X., Forbes, J. M., Hagan, M. E., Russell III, J. M., Palo, S. E., Mertens, C. J., & Mlynczak, M. G. (2006). Monthly tidal temperatures 20–120 km from TIMED/SABER. *Journal of Geophysical Research*, *111*, A10S08. https://doi.org/10.1029/2005JA011504